AJNR

Clinical NMR Imaging of the Brain: 140 Cases

G. M. Bydder, R. E. Steiner, I. R. Young, A. S. Hall, D. J. Thomas, J. Marshall, C. A. Pallis and N. J. Legg

AJNR Am J Neuroradiol 1982, 3 (5) 459-480
http://www.ajnr.org/content/3/5/459

Clinical NMR Imaging of the Brain: 140 Cases

G. M. Bydder[1]
R. E. Steiner[1]
I. R. Young[2]
A. S. Hall[2]
D. J. Thomas[3]
J. Marshall[3]
C. A. Pallis[4]
N. J. Legg[4]

Cranial nuclear magnetic resonance (NMR) scans were performed on 13 healthy volunteers and 140 patients with a broad spectrum of neurologic disease and compared with x-ray computed tomography (CT) scans. The NMR scans included a variety of sequences reflecting proton density, blood flow, T_1, and T_2 as well as transverse, sagittal, and coronal images. White matter, gray matter, and cerebrospinal fluid were clearly distinguished in the normal brain with inversion-recovery (IR) sequences, and normal progressive myelination was demonstrated in infants and children.

Acute hemorrhages displayed short T_1 values, but other pathologic processes such as infarction, infection, demyelination, edema, and malignancy were associated with long T_1 values. Cysts had very long T_1 values (about that of cerebrospinal fluid). Spin-echo (SE) sequences showed increased values of T_2 in a variety of conditions and highlighted lesions against the relatively featureless background of the remaining brain. With inversion-recovery scans, different stages of infarction were recognized in the hemispheres. NMR was more useful than CT in demonstrating brainstem infarction.

The white matter lesions in demyelinating diseases were well demonstrated with NMR scans. Many more lesions were observed in multiple sclerosis with NMR than with CT. Benign tumors were well seen and usually had shorter T_1 values than malignant tumors. Mass effects from tumors were generally better demonstrated with NMR than with CT, including more subtle mass effects such as displacement of the external capsule. Abnormalities were seen in diseases of the basal ganglia, including marked atrophy of the head of the caudate nucleus in Huntington chorea.

Advantages of NMR imaging include the high level of gray–white matter contrast, lack of bone artifact, variety of possible sequences, transverse, sagittal, and coronal imaging, sensitivity to pathologic change, and lack of known hazard. Disadvantages include lack of bone detail, limited spatial resolution, lack of contrast agents, and cost. Promising directions for future clinical research include developmental neurology, tissue characterization with T_1 and T_2, assessment of blood flow, and the development of contrast agents. Much more detailed evaluation will be required, but NMR seems to be a potentially important addition to existing techniques of neurologic diagnosis.

This article appears in the August 1982 issue of *AJR* and the September/October 1982 issue of *AJNR*.

Received March 18, 1982; accepted April 16, 1982.

[1]Department of Diagnostic Radiology, Royal Postgraduate Medical School, Hammersmith Hospital, Du Cane Road, London W12 0HS, England. Address reprint requests to R.E. Steiner.

[2] Picker International, Wembley, London, England.

[3] Institute for Neurology and National Hospital for Nervous Diseases, Queen Square, London, England.

[4] Department of Medicine (Neurology), Royal Postgraduate Medical School, Hammersmith Hospital, London, England.

***AJNR* 3:459–480, September/October 1982**
0195–6108/82/0305-0459 $00.00

Although NMR imaging was initially proposed in the United States [1, 2], much of the early development was carried out by small groups of physicists and engineers in Britain based at the Department of Bio-medical Physics in Aberdeen [3], the Department of Physics in Nottingham [4], and the Central Research Laboratories of Thorn-EMI Ltd. The hitherto published results of NMR imaging of the brain largely reflect the activities of these groups, although major contributions are expected from other centers in the near future. Head images were produced by the Thorn-EMI group in 1978 [5], and a series of brain scans was published by the Nottingham group during 1980 [6–10]. The Aberdeen group produced normal head images in 1980 [11] and have described abnormal cases during 1981 [12]. Nevertheless the total volume of published cerebral cases remains small. Fewer than 40 cases have been described with the largest series a group of 10 patients with multiple sclerosis [13].

In previous studies we have emphasized the high level of gray–matter contrast

TABLE 1: **NMR Scanning Sequences**

Scanning Sequence	Duration of Scan Cycle (msec)	τ* (msec)	Principal Image Determinants
Saturation-recovery (90°-t_d-):			
SR_{1000}	1000	...	Proton density
SR_{300}	300	...	Proton density, blood flow
SR_{150}	150	...	...
SR_{75}	75	...	...
Inversion-recovery (180°-τ-90°-t_d-):			
$IR_{1400/400}$	1400	400	Proton density, T_1
$IR_{2400/800}$	2400	800	...
$IR_{1200/200}$	1200	200	...
Spin-echo (90°-τ-180°-τ-echo-t_d-):			
$SE_{1040/20}$	1040	20	Proton density, T_2
$SE_{1080/40}$	1080	40	...
$SE_{1160/80}$	1160	80	...

* τ = time period between radiofrequency pulse to invert magnetization and second radiofrequency pulse during recovery to rotate residual magnetization for imaging.

obtained with NMR imaging of the brain using an inversion-recovery sequence [14] as well as the lack of bone artifact in the posterior fossa and the variety of sequences available in NMR imaging [15]. In this article these basic findings have been evaluated in 13 normal individuals and 140 patients with a broad spectrum of neurologic disease in order to (1) establish a basis for image interpretation, (2) ascertain the distinctive features of NMR in a variety of conditions, (3) assess the relative merits of the technique, and (4) indicate directions for future clinical research.

Subjects and Methods

Ten adult volunteers (six men, four women) of mean age 49 years, were scanned in order to obtain values of T_1 for white matter, gray matter, and cerebrospinal fluid (CSF). The area of the head of the caudate nucleus in transverse section was also measured. Three normal children aged 5, 7, and 9 years were scanned and 140 patients (78 men, 62 women) of mean age 53 years (range, 7 weeks to 78 years) were studied. Permission was obtained from the Ethics Committee of the Royal Postgraduate Medical School, and informed consent was obtained in each case. All NMR examinations conformed to the guidelines for clinical NMR imaging issued by the National Radiological Protection Board [16].

All patients were either inpatients of, or attending outpatient clinics at, St. Mary's Hospital, London; King Edward VII Hospital, Windsor; the National Hospital Queen Square; or Hammersmith Hospital, London. The patients were clinically examined and had either been recently investigated or were in the process of investigation. The clinical diagnosis was provided by the clinician responsible and this was supplemented or amended as necessary when further information became available after surgery or additional investigation.

No specific patient preparation was used except for two infants, aged 7 weeks and 13 months, who were each given oral promethazine for sedation before their NMR examinations. No contrast agents were used for the NMR scans.

The NMR machine in the Central Research Laboratory of Thorn-EMI Ltd., located at Hammersmith Hospital, and basic scanning sequences have been described [14, 15, 17]. Saturation-recovery (SR), inversion-recovery (IR), and spin-echo (SE) sequences were used and are detailed in table 1. Sagittal and coronal images were also used. Computations from saturation-recovery and inversion-recovery sequences of the same slice of the brain were used to obtain numeric values for T_1 as described for the liver [17].

After 73 patients had been examined, the slice profile was modified producing an improvement in image quality due to better definition of the relevant slice. The width of the slice had been underestimated in previous studies where it was quoted as about 9 mm [14, 15]; it is now thought to be about 12 mm.

In general, volunteers and patients were positioned with Reid's baseline parallel to the imaging plane for transverse images, although for some examinations of the posterior fossa, an angle of $-10°$ to $-15°$ to this baseline was used in order to obtain less oblique transverse images of the brainstem.

In the adult volunteers, saturation-recovery, inversion-recovery, and three spin-echo sequences were used. In the patients, a greater variety of SR and IR sequences were used, including IR sequences with τ = 200 msec and τ = 800 msec (table 1). The total number of slices varied with the type of information required but did not exceed 16 in any given case. A typical value providing full coverage of the brain was 10–12 slices.

Two volunteers and all patients had x-ray computed tomographic (CT) scans performed on a Siemens Somatom 2 whole-body scanner operating at 125 kVp and 230 mAs with a scan time of 10 sec and a slice width of about 8 mm. Contrast enhancement with 30–100 ml of sodium and meglumine diatrizoate was administered for these examinations as clinically indicated.

Results

Three patients who would otherwise have been included in this study felt sufficiently claustrophobic (either when first positioned in the NMR machine or after one or two slices) to request that the examination be stopped. No adverse effects were noted in the volunteers or other patients who completed their NMR examinations. Vomiting was induced in two patients with intravenous contrast material given during the CT examinations.

Technical Results

A variety of artifacts were noted on the NMR scans. A small central artifact was present on most scans; it was circular, sharply defined, and either black or white. Around the periphery of the image, linear artifacts were often noted. While these artifacts were readily recognized, a loss of gray-white contrast on the left side of the image temporarily produced by a defect in one of the gradient coils was less obvious.

Minor movement produced a general blurring of the image with fair preservation of underlying detail, but gross movement produced images of little or no value. Curvilinear, wavelike and band-shaped artifacts due to effects from tissue outside the scan plane were seen in early images but were eliminated by the use of additional Z gradients in later scans. A decrease in pixel values toward the upper part of the imaging field due to field nonhomogeneity was also noted. Spin-echo images were less susceptible to variations in the field than inversion-recovery images.

Small quantities of iron outside the slice (such as safety

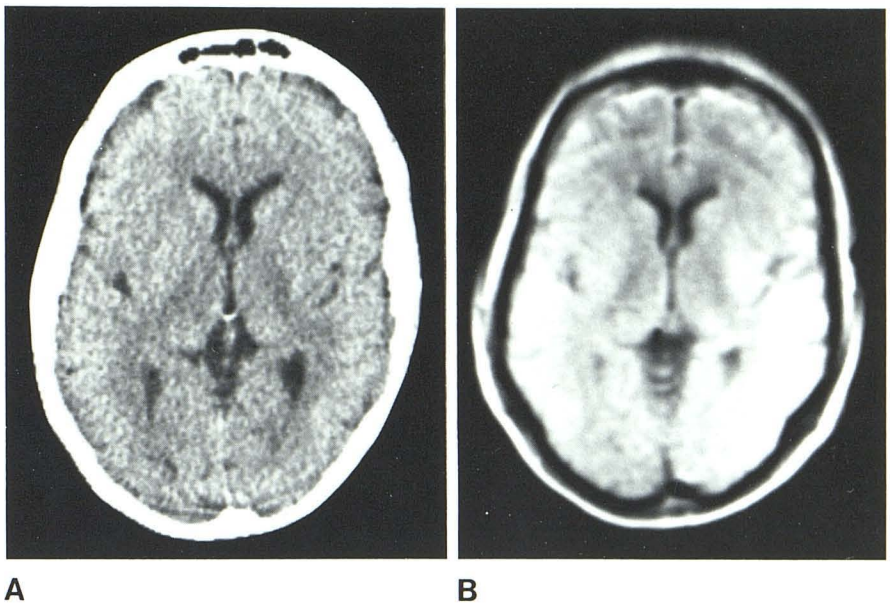

Fig. 1.—Normal adult brain at low ventricular level (49-year-old male volunteer). **A**, CT. **B**, SR_{1000} scan: relatively featureless.

pins and bra or suspender fasteners at shoulder level) produced black, inverted, U-shaped artifacts. Smaller but similar artifacts were produced by stainless steel clips and ventricular shunt valves within the imaging plane in some cases, but no artifact whatsoever was produced by these materials in other instances. Less specific artifacts (including noise, mottle, and streaking) were also seen.

Normal Appearances

Saturation-Recovery (SR) Images

The saturation-recovery image reflects proton density (ρ), with areas of increased proton density appearing toward the light end of the gray scale and areas with low proton density at the dark end. Thus subcutaneous fat and brain, both with a high proton density, appear white or light gray but the inner and outer tables of the skull, with a low proton density, appear dark. Little or no gray–white matter contrast is seen with SR images (fig. 1B).

An exception to this general pattern is CSF which, despite its high proton density, appears dark. Because of its long relaxation time (about 1500 msec), the magnetization of CSF recovers incompletely before the next 90° pulse 1000 msec later. This pulse thus rotates a reduced magnetization vector leading to a small detected signal and thus a dark appearance [15].

Blood, having a high proton density, appears white (as in the superior longitudinal sinus in fig 1B). When the duration of the sequence cycle is decreased with the SR_{300}, SR_{150}, and SR_{75} sequences, blood flowing into the slice is highlighted [15]. SR sequences were used to demonstrate flow effects, to highlight regions with a very long T_1, and to demonstrate the presence of fluid. In combination with IR images, these scans were also used to calculate tissue T_1 values.

Inversion-Recovery (IR) Images

Unlike SR images, IR images with the 1400/400 sequence appear to display optimum gray–white matter contrast [18] (fig. 2A). Images of this type show three distinct tissue levels. White matter, which has a short T_1 value, appears white and is clearly seen from the central regions of the brain to the subcortical areas. Gray matter, which has a longer T_1 value, appears gray and its extent is defined by surrounding CSF and white matter. CSF has a very long T_1 value and appears black. Tissue levels displayed on the gray scale using this sequence are summarized in table 2, and numerical values for T_1 for the brain obtained from the 10 normal adult volunteers are shown in table 3.

IR images showed some similarity to CT images, but the high level of gray–white matter contrast and low signal from cortical bone produced a number of differences. Because of the three basic levels on the gray scale for NMR (white matter, gray matter, and CSF) rather than the two of CT (brain and CSF), window width and level settings required to achieve satisfactory overall levels of contrast and brightness were more restricted. Optimum settings for display of a particular lesion often resulted in inadequate display of the background anatomic detail.

Differences in features of the partial-volume effect were also noted. Whereas with CT, partial-volume effects occur at the interface between brain and CSF or bone, IR images also display partial-volume effects at the margin between gray and white matter. In particular, partial-volume effects from the gray matter of cerebral sulci may produce an apparent long T_1 lesion within white matter. Partial-volume effects from bone produce a general darkening of the brain within the slice but with good preservation of gray–white matter contrast. Small proportions of CSF within the slice produce quite significant partial volume effects within the brainstem. As a result the pontomedullary junction may be

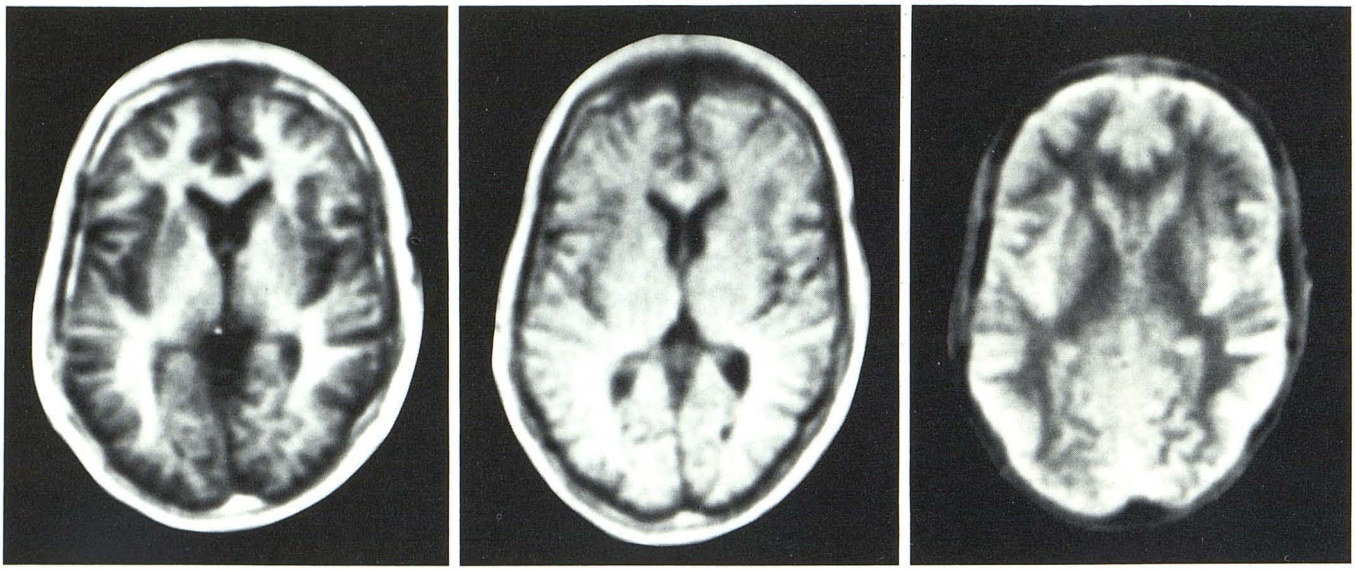

Fig. 2.—Normal adult brain at low ventricular level (49-year-old male volunteer). **A**, $IR_{1400/400}$ scan: high level of gray–white matter contrast. **B**, $IR_{2400/800}$ scan: less contrast. **C**, $IR_{1200/200}$ scan: almost appears to be negative of $IR_{1400/400}$ scan (**A**).

TABLE 2: **Tissue Gray-Scale Levels ($IR_{1400/400}$ Sequence)**

Typical Gray-Scale Levels	Tissue
White	Subcutaneous fat and bone marrow, white matter
Gray	Gray matter, muscle
Black	Blood vessels, air, cortical bone, CSF

TABLE 3: **Normal T_1 Values ($IR_{1400/400}$ Sequence)**

Tissue or Fluid	Range of mean T_1 Values (msec)
White matter:	
Forceps minor	220–350
Forceps major	240–350
Gray matter:	
Caudate nucleus	440–590
Lenticular nucleus	380–480
Thalamus	340–410
Insular cortex	480–600
Cerebral cortex	440–610
Cerebrospinal fluid: frontal horns	900–2000*

* Upper limit of scale.

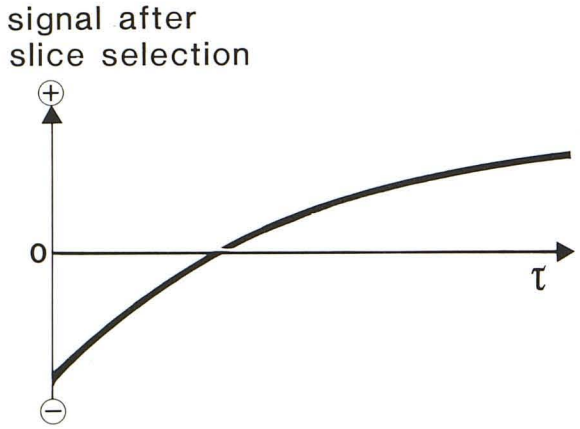

Fig. 3.—Variation of total signal with τ after slice selection using IR sequence.

seen as a curvilinear dark narrow band within the slice following the contour of the lateral aspect of the upper medulla, and the pontomesencephalic junction may appear as a narrow linear band on either side of the brainstem.

The hemisphere asymmetries seen with CT, such as relative enlargement of left parietooccipital and right frontal regions [19], are well demonstrated. The high level of gray–white matter contrast enables the insular cortex and external capsule to be clearly defined. As a result lesser asymmetries tending to parallel those of the hemispheres as a whole are seen in these regions.

The external anatomy of the brainstem as seen with CT cisternography [20] provides a useful guide to the external aspects of the brainstem on NMR images. Within the brainstem, the normally situated deep gray matter of the red nucleus, substantia nigra, pontine, and mesencephalic nuclei were recognized. The boundary between cerebellum and occipital cortex is well defined by the quite different patterns of the cerebellar folia and the occipital sulci.

The $IR_{1400/400}$ sequence was used routinely for most diagnostic purposes, but two further IR sequences, $IR_{2400/800}$ and $IR_{1200/200}$, were used in particular cases. $IR_{2400/800}$ images (fig. 2B) show much less gray–white matter contrast than those with the $IR_{1400/400}$ sequence, but the difference

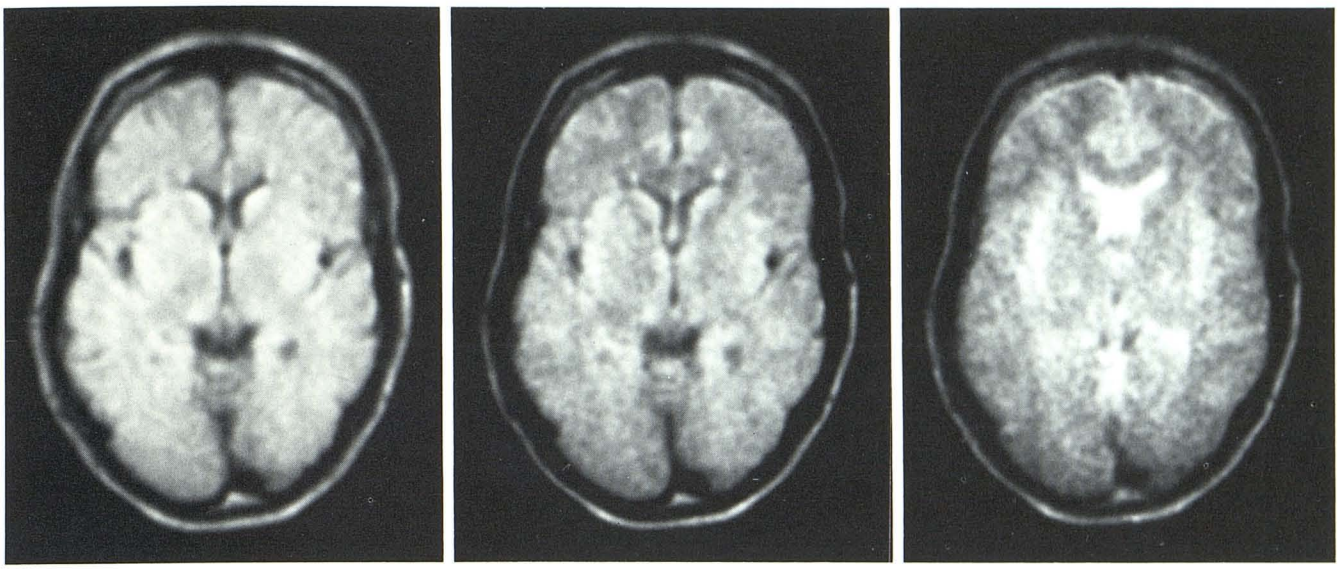

Fig. 4.—Normal adult brain at low ventricular level (49-year-old male volunteer). **A**, $SE_{1040/20}$ scan. **B**, $SE_{1080/40}$ scan. **C**, $SE_{1160/80}$ scan. All SE scans become noisier but begin to show more gray-white matter contrast as τ is increased from 20 msec (**A**) to 80 msec (**C**).

between gray matter and CSF is well seen. This sequence was used to highlight differences among lesions with long T_1 values, such as malignant tumors and cerebral edema.

$IR_{1200/200}$ images (fig. 2C) differ radically from $IR_{1400/400}$ images (fig. 2A), since white matter appears gray, gray matter appears white, and CSF appears white, although low-proton-density areas such as the inner and outer tables of the skull remain dark with both sequences. With the IR sequence, if τ is long compared to the average T_1 of tissue in the slice, the average longitudinal magnetization almost recovers to its equilibrium value at time τ after the 180° pulse and the total signal from the slice after slice selection is large and positive (fig. 3). If τ is short compared to the average T_1 of tissue in the slice, the average longitudinal magnetization recovers only slightly and the signal after slice selection is negative. Hence there is an intermediate critical value of τ for which the total signal after slice selection is zero. This critical value depends on the nature of the tissue in the slice. As a result of the particular method of data processing used for image reconstruction in this study, images with τ below this critical value appear roughly like negatives of images with τ above it.

$IR_{1200/200}$ scans were used to distinguish areas with a long T_1 from those with a low proton density, both of which appear dark on $IR_{1400/400}$ scans. On the $IR_{1200/200}$ scan, however, the long T_1 region appears light and the low-proton-density region remains dark. This was of value in demonstrating peripheral lesions and areas adjacent to or involving bone. It was also used to check possible artifacts seen with the $IR_{1400/400}$ sequence.

Problems were experienced in obtaining regions of interest that represented pure white or gray matter on T_1 scans derived from SR and IR scans because of partial-volume effects. The cerebral cortex not only follows a complex folded contour, but is usually less than 5 mm thick. With a scan slice thickness of about 12 mm, difficulty in sampling cortical gray matter was unavoidable. The same considerations applied to white matter and CSF.

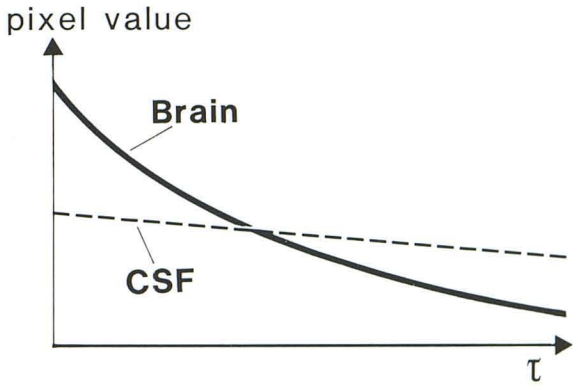

Fig. 5.—Variation of pixel values of brain and CSF with τ using SE sequence.

Spin-Echo (SE) Images

$SE_{1040/20}$, $SE_{1080/40}$, and $SE_{1160/80}$ images are shown in figure 4. As τ is increased, the SE images became noisier due to a drop in signal strength. Little contrast between gray and white matter is evident with τ = 20 msec, but greater contrast is seen as τ is increased to 80 msec. With SE images, tissues with a short T_2 usually appear dark and those with a long T_2 generally appear light (unlike tissues with a long T_1 on $IR_{1400/400}$ images which appear dark). Thus in the subject shown in figure 4C, white matter with a shorter T_2 value appears darker than gray matter.

While CSF appears darker than brain in the $SE_{1040/20}$ and

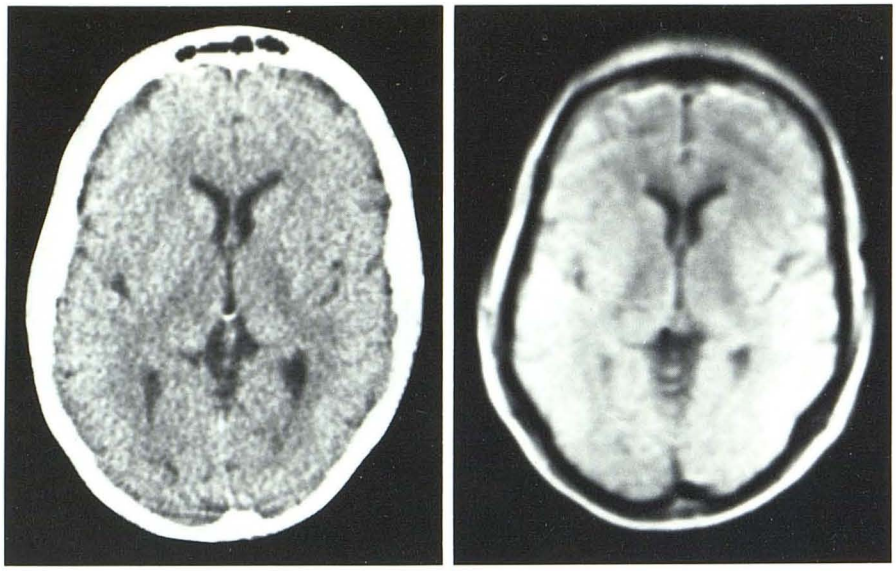

Fig. 6.—Images in figs. 1, 2, and 4 are reassembled here for reader's convenience. They are of same anatomic level in same individual. Wide diversity of patterns deriving from different imaging sequences is impressive.

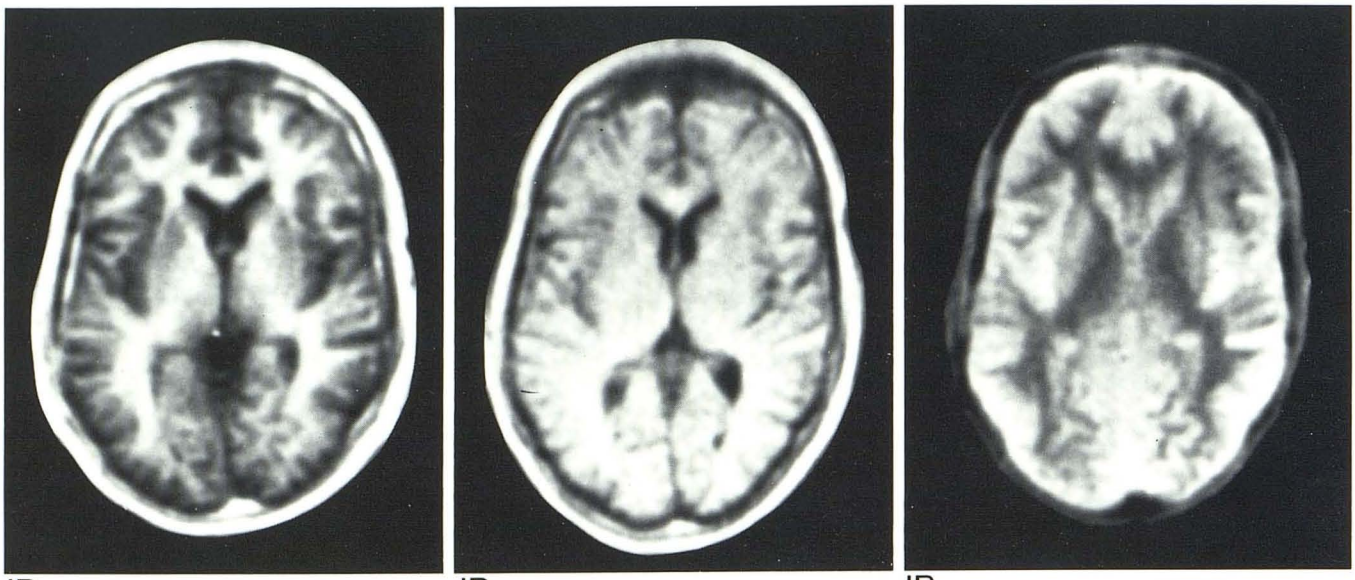

$IR_{1400/400}$ $IR_{2400/800}$ $IR_{1200/200}$

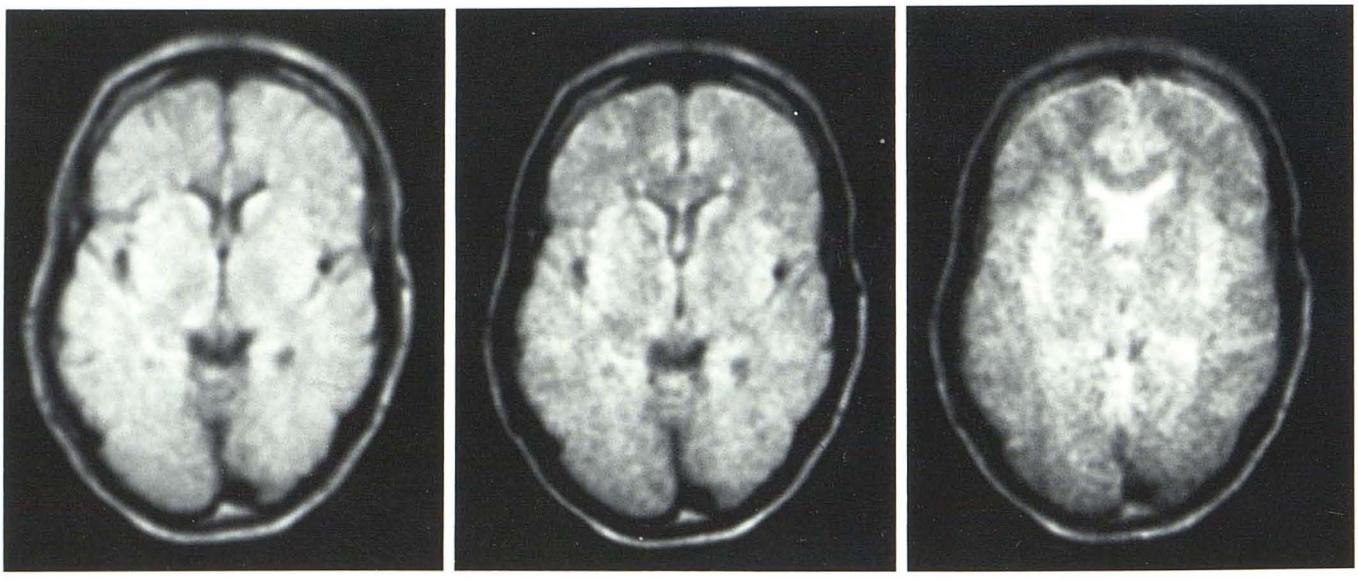

$SE_{1040/20}$ $SE_{1080/40}$ $SE_{1160/80}$

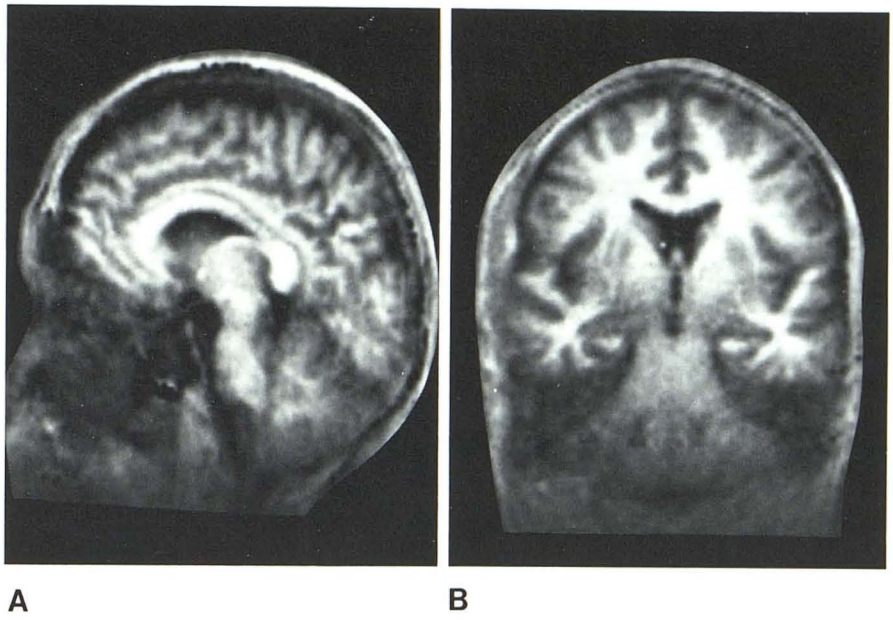

Fig. 7.—Normal adult brain (37-year-old volunteer). Sagittal (**A**) and coronal (**B**) $IR_{1400/400}$ images. Gray- and white-matter contrast is seen, although images are noisier than transverse scans.

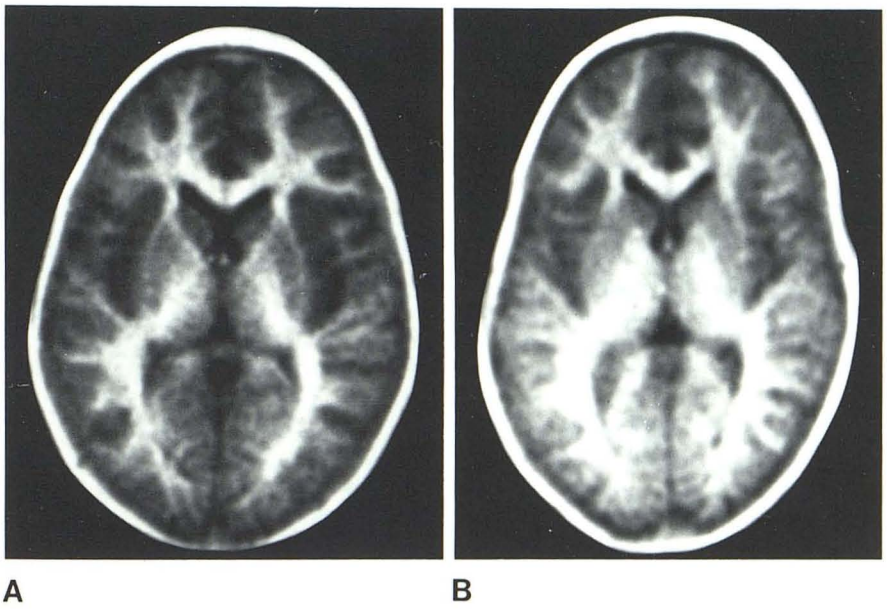

Fig. 8.—Normal brain $IR_{1400/400}$ images in children aged 5 (**A**) and 9 (**B**) years. Less white matter evident that in adults, although there is increase from **A** to **B**.

$SE_{1080/40}$ scans, it appears lighter on the $SE_{1160/80}$ scan. CSF and brain have numerically similar proton densities and so have similar longitudinal magnetizations at equilibrium. Since T_1 of CSF is much longer than that of either gray or white matter, the recovery of the longitudinal magnetization toward its equilibrium value is slower for CSF than for brain. Hence immediately before the 90° pulse, the longitudinal magnetization in CSF is less than that in brain, and after this pulse the same applies to the transverse magnetization. However, since T_2 of CSF is also much longer than T_2 of brain, the transverse magnetization of CSF decays more slowly than that of brain (fig. 5). The pixel value at a point in a spin-echo image is proportional to the transverse magnetization at the time of the echo at the corresponding point. Hence for small values of τ, pixel values of CSF are greater than those of brain, but as τ is increased the pattern reverses.

SE sequences with a long τ were of particular value in demonstrating acute and space-occupying lesions as well as cerebral edema.

For ease of comparison of SR, IR, and SE techniques, figures 1, 2, and 4 are assembled in figure 6.

Sagittal and Coronal Scans

Sagittal and coronal scans using the $IR_{1400/400}$ sequence are illustrated in figure 7. Gray- and white-matter contrast is seen as with transverse scans, although the images are

noisier. Sagittal scans were mainly used to demonstrate brainstem relations and midline lesions. Coronal scans were generally used to demonstrate the anatomic relations of deep-seated lesions.

Higher resolution scans produced by an increase in the gradient fields were used in both infants and the three children included in the series. Normal $IR_{1400/400}$ scans of children aged 5 and 9 years are shown in figure 8. The degree of myelination is greater in the elder child but less than that seen in adults.

Pathologic States

The diagnostic entities in 140 patients are detailed in table 4.

Cerebral Infarction

Cases have been separated into hemisphere (30 cases) and brainstem (13) groups. The hemisphere group has been further subdivided into acute (nine cases), chronic (17), lacunar (four), and hemorrhagic (two). Loss of gray–white matter contrast alone is also considered as a possible feature of infarction or ischemia.

Hemisphere infarcts were identified in patients with other conditions including brainstem infarcts, meningitis, multiple sclerosis, tumors, Parkinson disease, Huntington chorea, and cerebellar atrophy.

The earliest infarction was seen within 1 day of its onset. In cases of acute infarction, $IR_{1400/400}$ images displayed a well defined region of loss of gray–white matter contrast with a T_1 value greater than that of gray matter (fig. 9). Mass effects, including compression of sulci and displacement of the ventricular system, were generally seen as with CT scans, but more subtle mass effects, such as displacement of the external capsule, were only seen with IR scans. SE scans displayed areas of increased T_2 corresponding in position to the lesions seen with IR scans and CT (fig. 10). SR images displayed mass effects and a small increase in proton density, but this was too indefinite to define the boundaries of the infarct. Infarcts were seen in deep and superifical distributions. The overall correspondence with the CT scan appearances was excellent.

Chronic infarcts were defined as those of at least 2 months duration. The characteristic feature was a well defined region of loss of gray–white contrast with a long or very long T_1 value (fig. 11). Widening of sulci and enlargement of the ipsilateral ventricle were seen as with CT. SR_{1000} scans showed dark regions due to the very long T_1 of cystic components in chronic infarction rather than slightly lighter areas due to increased proton density seen in acute cases. The infarcts were generally peripheral and often wedge shaped.

Lacunar infarcts were generally circular and usually multiple. The general features of loss of gray–white matter contrast and increased T_1 were again seen, although the loss of contrast was not apparent in lesions confined to gray or white matter alone. The lesions were deep seated and were well seen with CT.

TABLE 4: **Clinical Diagnoses**

Diagnosis	No.
Cerebral infarction*:	
Hemisphere†	30
Brainstem	13
Intracranial hemorrhage:	
Intracerebral	4
Subdural	1
Other vascular disease:	
Giant aneurysm	2
Arteriovenous malformation	1
Cerebral trauma	2
Intracranial infection:	
Meningitis	2
Cerebral abscess	2
Subdural abscess	1
Neurosyphylis	2
Demyelinating disease:	
Multiple sclerosis	13
Binswanger disease	2
Hydrocephalus‡	4
Benign tumors:	
Meningioma	4
Acoustic neuroma	3
Prolactinoma	1
Malignant tumors:	
Glioma	4
Metastasis	12
Diseases of the basal ganglia:	
Parkinson disease	4
Huntington chorea	2
Wilson disease	2
Congenital and inherited disease:	
Tuberosclerosis	1
Hereditary ataxias	3
Congenital malformations	2
Craniovertebral anomalies	1
Atrophic disease:	
Primary cerebral atrophy	7
Primary cerebellar atrophy	2
Motor neuron disease	4
Other diseases	9
Normal subjects	13

* Cerebral infarction was detected in patients who also had intracranial hemorrhage, meningitis, multiple sclerosis, tumors, Parkinson disease, Huntington chorea, and cerebellar atrophy.

† Includes two cases of hemorrhagic infarction.

‡ Hydrocephalus was associated with tumor in two cases.

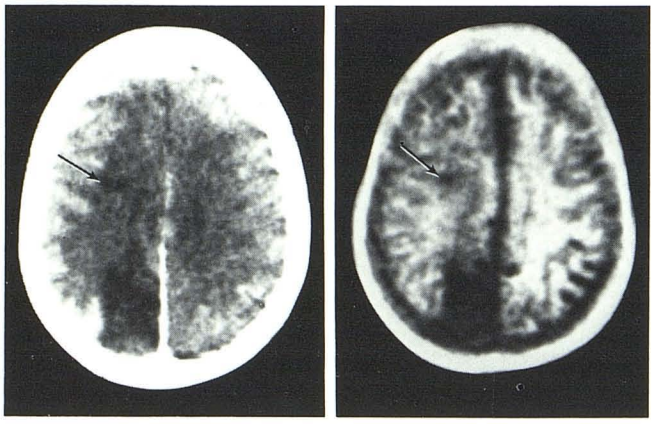

A B

Fig. 9.—Acute infarction. **A**, Contrast-enhanced CT. **B**; $IR_{1400/400}$. Infarct in occipital region seen on both scans. Possible small area of infarction (*arrows*) and some loss of gray-white matter contrast in left hemisphere (**B**).

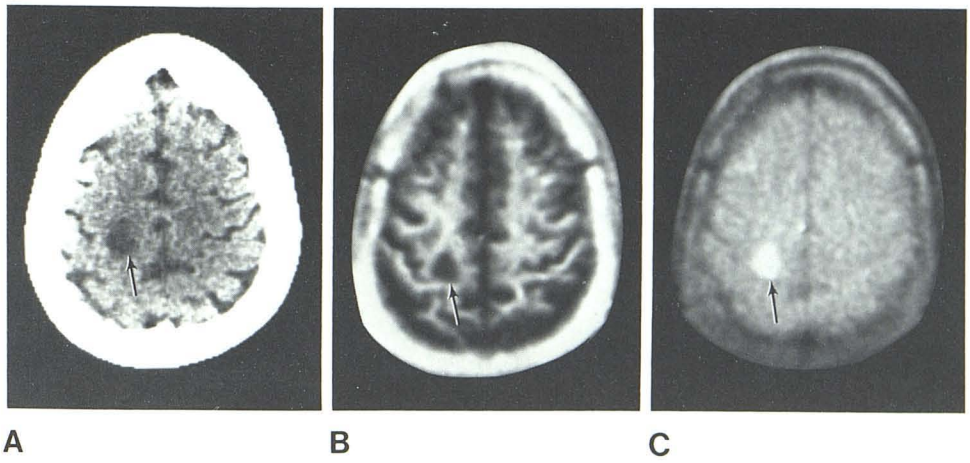

Fig. 10.—Acute infarction. **A**, CT. **B**, $IR_{1400/400}$. **C**, $SE_{1080/40}$. Area of infarction clearly defined on all three scans (*arrows*).

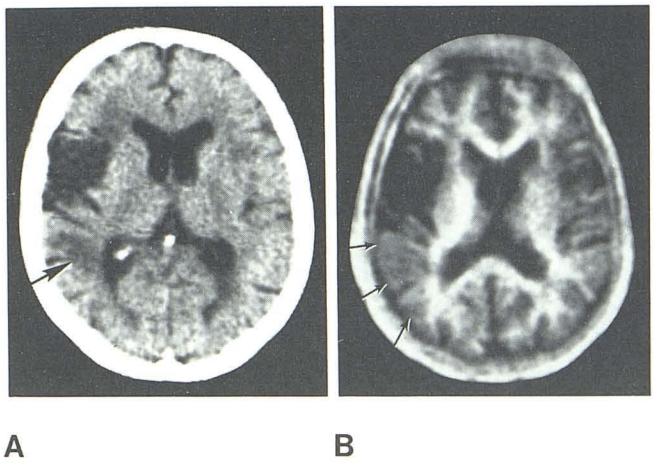

Fig. 11.—Chronic infarction. **A**, CT. **B**, $IR_{1400/400}$. Most of infarcted area seen as long T_1 region on **B**. However, smaller region with loss of gray–white matter contrast alone posterior to this region (*small arrows*) corresponds to smaller area of infarction on CT scan (*large arrow*).

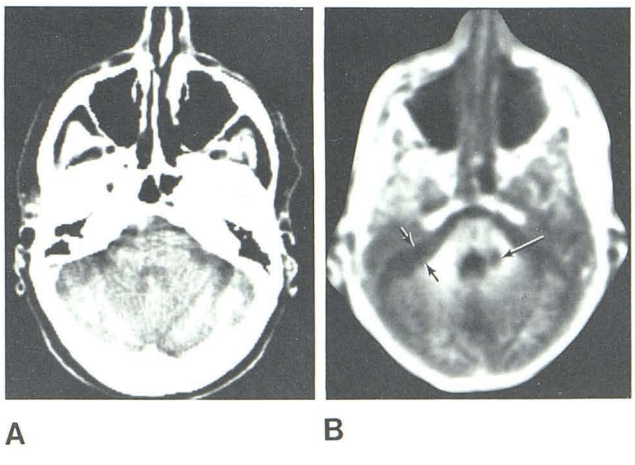

Fig. 12.—Brainstem infarction and cerebellar atrophy. **A**, CT. **B**, $IR_{1400/400}$. Area of infarction appears dark (*long arrow*). Significant CSF seen between petrous bone and anterior margin of cerebellum possibly related to cerebellar hemisphere atrophy (*short arrows*).

Thirteen cases of clinical brainstem infarction were examined. In 10, lesions were identified with $IR_{1400/400}$ scans. Infarction was manifested as a well defined region with a long T_1 (fig. 12). Circular, linear, and branching patterns were seen, and these were often multiple. Sparing of a rim of brainstem immediately below the surface was often seen, possibly corresponding to the territory of the circumferential arteries. Cerebellar involvement was seen in three cases and was most obvious on $IR_{1400/400}$ scans when it involved the white matter of the cerebellar peduncles.

Two cases of hemorrhagic infarction were studied, both in patients with cardiac arrhythmias receiving anticoagulants in whom embolism was strongly suspected. The $IR_{1400/400}$ sequence showed a combination of features seen in infarction and in hemorrhage. The infarct was defined by its long T_1 and loss of gray–white matter contrast; but within the area of infarction, a region with a short T_1 corresponded to the area of hemorrhage shown with CT (fig. 13). In addition,

Fig. 13.—Hemorrhagic infarction. **A**, CT. **B**, $IR_{1400/400}$. Area of hemorrhage displays short T_1 rim with longer T, center. Additional areas of infarction are noted.

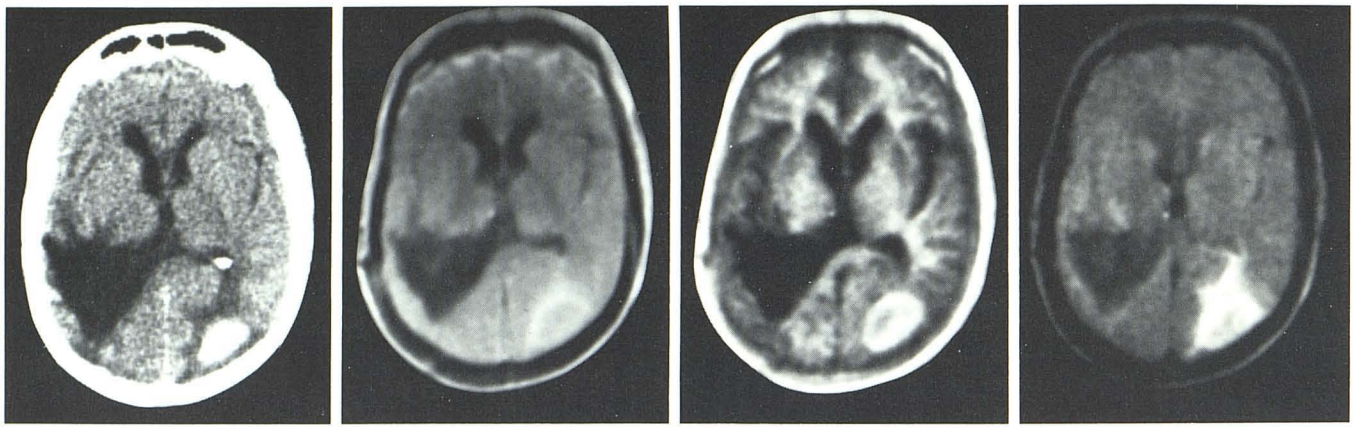

Fig. 14.—Intracerebral hemorrhage. **A**, CT. **B**, SR_{1000}. **C**, $IR_{1400/400}$. **D**, $SE_{1080/40}$. Areas of hemorrhage and edema demonstrated on right. Porencephalic cyst on left.

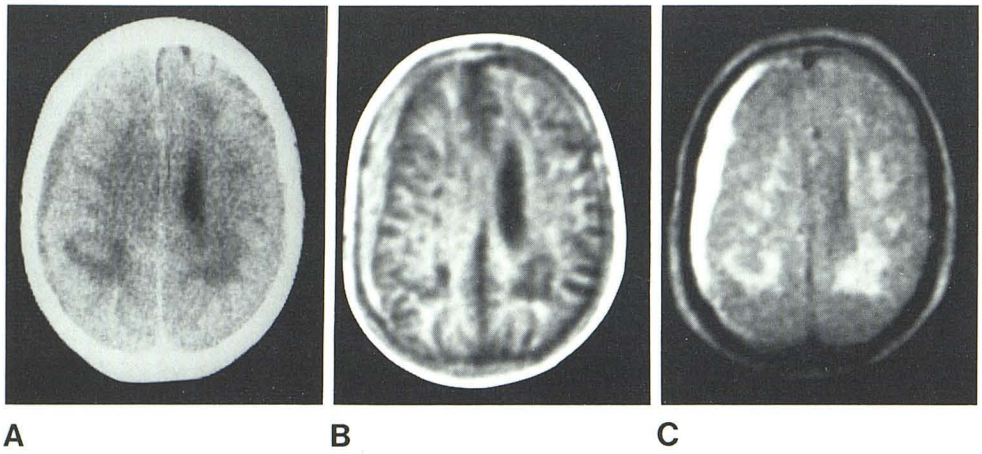

Fig. 15.—Subdural hemorrhage. **A**, CT. **B**, $IR_{1400/400}$. **C**, $SE_{1080/40}$. Hemorrhage demonstrated on all three scans.

the $IR_{1400/400}$ scan showed a darker region with a longer T_1 within the hemorrhage.

Loss or diminution of gray–white matter contrast without an accompanying overall increase in T_1 was seen in five cases. This was manifested as slightly less contrast in the hemisphere involved without CT change in one case (fig. 9). In two other cases, loss of gray–white matter contrast was seen in an area adjacent to the increased T_1 area and was associated with evidence of infarction on the CT scan (fig. 11). In three other cases, loss of contrast was seen without significant CT change, as has been reported [14].

Intracranial Hemorrhage

Five cases of intracranial hemorrhage were examined; four of these were intracerebral hemorrhage, observed 4, 8, 17, and 22 days after onset. In one case, the intracerebral hemorrhage extended into the subarachnoid space. All four cases showed a partial or complete rim of shorter T_1 and a central region of longer T_1 (fig. 14). This feature was most marked in the hemorrhage of 22 days duration. Long T_2 regions were also seen. In one case, followed for 7 months after the original scan, examination showed almost complete resolution with a small persisting low attenuation region on CT and a long T_1 area on NMR. All hemorrhages were surrounded by edema, and mass effects were clearly demonstrated. Although the hemorrhages were clearly seen with CT, the rim and central area were not shown. Subarachnoid extension was seen in one case with blood identified (because of its short T_1) within cerebral sulci.

In a case of subdural hemorrhage examined 13 days after a head injury, hemorrhage, mass effect, and edema were clearly demonstrated with NMR. The SE images were particularly striking (fig. 15).

Other Vascular Diseases

Two patients with giant aneurysms were studied. Both showed short T_1 regions within the aneurysm as previously described [14]. In one patient, a large arteriovenous malformation was seen as a region of long T_1 with $IR_{1400/400}$ scans (fig. 16B). Using flow-dependent SR sequences, vessels

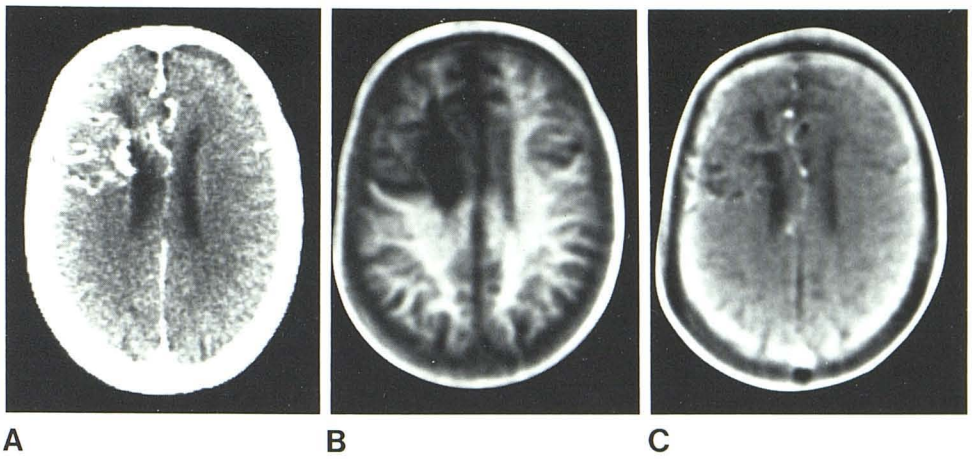

Fig. 16.—Arteriovenous malformation. **A**, Contrast-enhanced CT. **B**, $IR_{1400/400}$. **C**, SR_{300}. Vessels with significant flow into slice seen on SR_{300} scan (**C**), and lesion appears as region of long T_1 on $IR_{1400/400}$ scan (**B**). Loss of gray–white matter contrast seen in abnormal area.

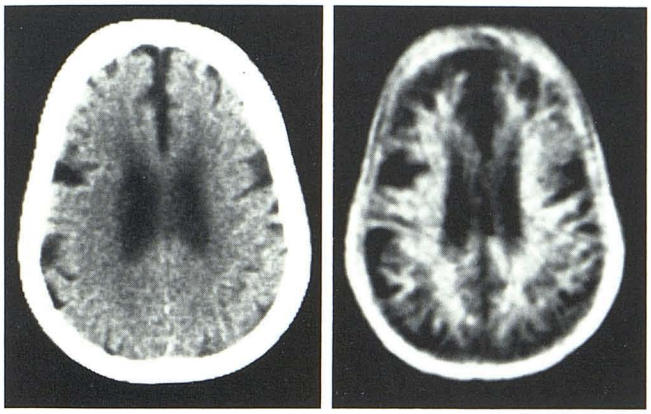

Fig. 17.—Tuberculous meningitis. **A**, CT. **B**, $IR_{1400/400}$. Areas of infarction demonstrated with both scans. In addition, cerebral white matter appears to "merge" with bone marrow.

with significant flow into the slice were demonstrated (fig. 16C).

Trauma

In both cases studied, loss of brain was demonstrated in a similar way to that seen with CT. Loss of gray–white matter contrast was evident within the temporal lobe of the right hemisphere, below the site of impact in a patient examined 4 months after injury, although the CT scan in this area displayed no abnormality. Long-T_1 lesions were also seen within the pons of this patient.

Intracranial Infection

Two cases of tuberculous meningitis and two cases of tuberculous abscess were studied. One case with a subdural empyema and two patients with neurosyphylis were also examined.

No abnormality was detected in one case of meningitis. In the second, several peripheral areas of infarction were demonstrated with both CT and NMR. In addition, the peripheral white matter appeared to extend laterally and "merge" with the bone marrow (fig. 17). This appearance was possibly due to compression or loss of cortical gray matter or the presence of exudate in the subarachnoid space (or a combination of both these processes).

In both cases of tuberculous abscess, long T_1 areas on NMR corresponded to the abnormality seen with CT. Mass effects were well demonstrated on the NMR scan. Follow-up in one case after chemotherapy showed considerable resolution of the abscess (fig. 18).

In a patient with subdural empyema, both CT and $IR_{1400/400}$ scans demonstrated the fluid collection and associated empyema. After surgery, the CT scan showed slight compression of adjacent sulci, although an $IR_{1400/400}$ scan showed evidence of residual fluid or organizing tissue as well (fig. 19).

In one case of neurosyphylis, selective gray matter loss was demonstrated as well as areas of peripheral infarction (fig. 20).

Demyelinating Disease

Thirteen probable or established cases of multiple sclerosis were studied as well as two of Binswanger disease.

In multiple sclerosis, lesions were observed in the periventricular white matter as well as in the brainstem and cerebellum with both $IR_{1400/400}$ and $SE_{1080/40}$ scans (fig. 21). Nine total lesions were detected by CT, compared with a total of 53 with NMR using previously described criteria [13].

Of particular interest was a patient with probable multiple sclerosis who had an acute left hemiplegia. A large lesion was demonstrated with NMR; follow-up showed diminution (fig. 22). In another patient with probable multiple sclerosis, who had left facial myokymia, a lesion was demonstrated in the pons anterolateral to the fourth ventricle (fig. 23).

In both cases of Binswanger disease, extensive white matter changes were demonstrated (fig. 24). Abnormalities

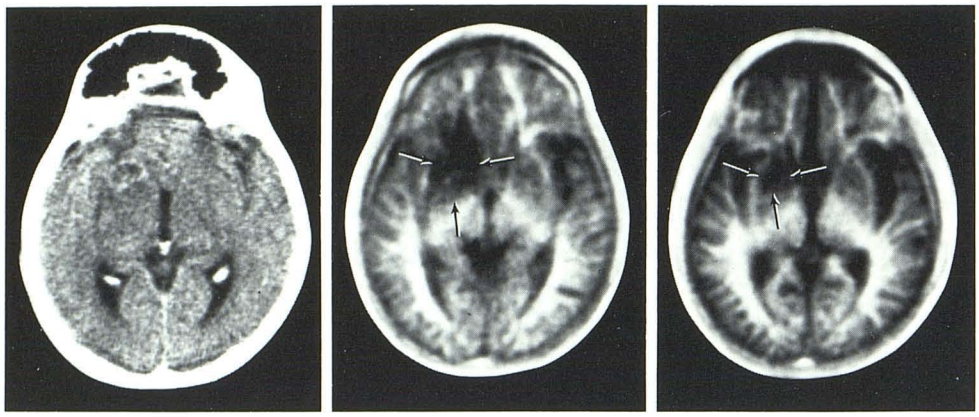

Fig. 18.—Tuberculous abscess. **A**, Contrast-enhanced CT. **B**, $IR_{1400/400}$. **C**, Follow-up $IR_{1400/400}$ 7 months later. Abnormal area has long T_1 and is smaller on follow-up scan (*arrows*).

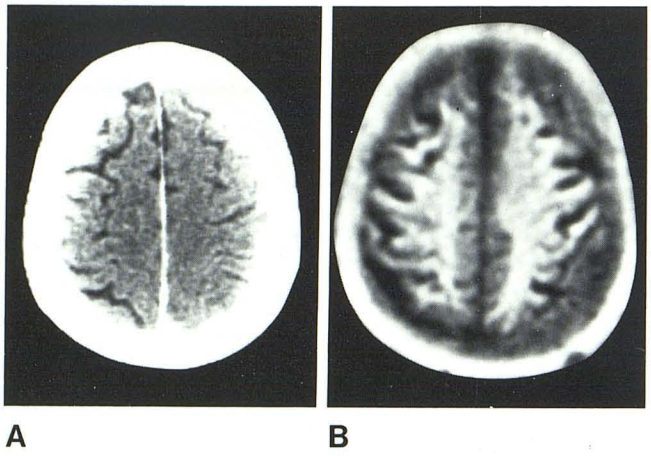

Fig. 19.—Subdural empyema after surgery. **A**, Contrast-enhanced CT. **B**, $IR_{1400/400}$. Evidence of sulcal compression on right on CT scan (**A**). Residual fluid or tissue also seen on NMR scan (**B**).

were also seen on CT, but these were not as extensive as those seen with NMR.

Hydrocephalus

Enlargement of the ventricular system was seen as with CT. The margins of the ventricular system were well demarcated because of the high degree of contrast between white matter and CSF. One case of suspected normal-pressure hydrocephalus was studied, but the other cases were associated with tumors. In patients with hydrocephalus due to tumor, increased T_2 regions were seen at the margins of the ventricular system (fig. 25).

Long T_1 regions corresponding to the CT appearances of periventricular lucency were demonstrated in the case of suspected normal-pressure hydrocephalus.

Benign Tumors

Four patients with meningiomas, three with acoustic neuromas, and one with a prolactinoma were examined. T_1 values for seven of these tumors are shown in table 5. The T_1 values were generally shorter than those of malignant tumors, although there was some overlap and a cystic acoustic neuroma had a very long T_1 value. T_2 values were increased in two cases and increased proton density was seen in three cases. All tumors were demonstrated with both CT and NMR scans (fig. 26). Edema was generally minimal. Mass effects were well demonstrated with NMR (fig. 27).

Malignant Tumors

Four gliomas and 12 cases of metastatic cancer were studied. The gliomas included astrocytoma grade 2 (two cases) and glioblastoma multiforme (two cases). The T_1 values were generally increased (table 5). In five cases, the tumor was clearly separated from the surrounding edema with $IR_{1400/400}$ scans (fig. 28), but difficulty in defining this margin was experienced in the remaining nine patients, although the use of the $IR_{2400/800}$ sequence was of value in this situation (fig. 29). SE sequences were also useful in defining the extent of associated cerebral edema as well as tumors (fig. 30). Contrast-enhanced CT was of particular value in separating tumor from surrounding edema, whereas mass effects were better displayed with NMR. A possible metastasis was seen in the brainstem, although this was not demonstrated with CT (fig. 31).

Diseases of the Basal Ganglia

In this group of diseases, involuntary movement produced less image degradation than with CT. Using $IR_{1400/400}$ scans, the substantia nigra was usually seen in normal volunteers. It was positively identified in one patient with Parkinson disease but not in another two. In a patient with unilateral Parkinson disease probably of post encephalitic origin, a long T_1 lesion was seen in the upper mesencephalon (fig. 32). In a patient treated for Parkinson disease with bilateral thalamotomy (which was followed by pseudobulbar palsy), two long T_1 lesions were seen within the thalamus. Cerebral atrophy was seen with both NMR and CT in a further case of Parkinsonism.

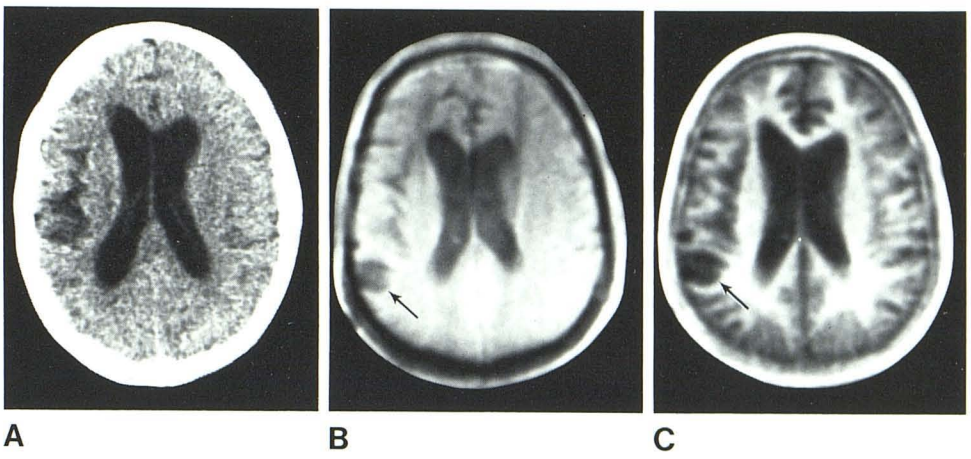

Fig. 20.—Neurosyphylis. **A**, CT. **B**, SR_{1000}. **C**, $IR_{1400/400}$. Loss of gray matter in medial aspect of frontal lobe and over insular cortex on left. Area of infarction (*arrows*) in left parietal area.

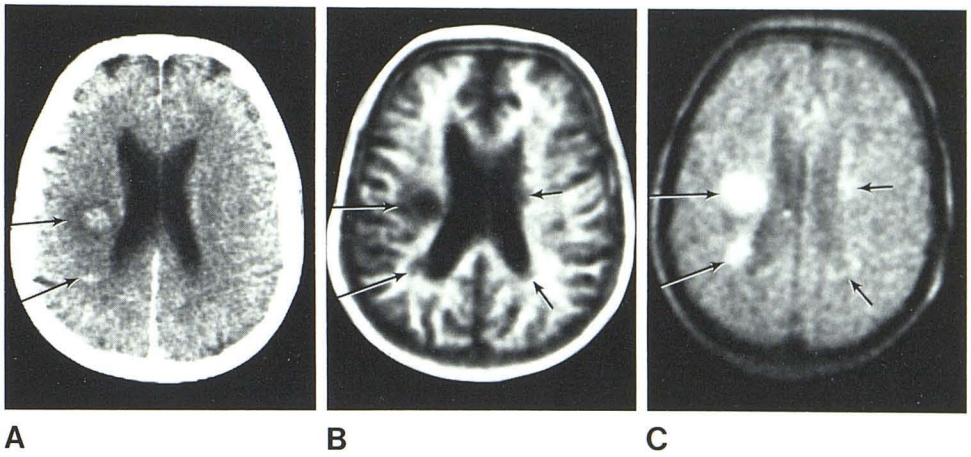

Fig. 21.—Multiple sclerosis. **A**, Contrast-enhanced CT. **B**, $IR_{1400/400}$. **C**, $SE_{1080/40}$. Contrast-enhancing lesions on CT scan (**A**) are seen with both NMR scans (*long arrows*). Two other lesions only demonstrated with NMR (*short arrows*).

Two patients aged 46 and 50 with 5 and 7 year histories of Huntington chorea, respectively, were examined. Marked atrophy of the heads of the caudate nuclei were seen in both cases (fig. 33), and the cross-sectional area of this nucleus could not be measured in transverse slices through the foramen of Monro.

In the 10 normal volunteers (mean age, 49 years), the area of the head of the caudate nucleus varied from 10 to 22 mm^2 in transverse slices of the same thickness through the same region.

Two cases of Wilson disease were examined. One showed an area of increased T_1 and T_2 in the lenticular nuclei (fig. 34). The other showed bilateral increased T_1 areas in the lenticular nuclei and thalami. The CT scans showed less well defined low attenuation areas in this case.

Congenital and Inherited Disease

Cases of tuberosclerosis, Friedreich ataxia, hemiatrophy (two), agenesis of corpus callosum, and Arnold Chiari malformation were examined. Calcified lesions were well demonstrated with CT in the case of tuberosclerosis. Lesions were also identified in the characteristic periventricular site with $IR_{1400/400}$ scans.

The case of Friedreich ataxia showed atrophy of the cerebellar vermis, which was also seen in a case of olivopontocerebellar degeneration. Both cases of hemiatrophy were demonstrated in a similar way to CT, as was the case of agenesis of the corpus callosum.

The patient with an Arnold Chiari malformation had been treated by surgical decompression for associated syringomyelia. The central canal appeared continuous with the cisterna magna. The patient with Sturge-Weber disease displayed loss of gray–white matter contrast outside the region of calcification seen with CT.

Atrophic Disease

Cases of cerebral atrophy, cerebellar atrophy, and motor neurone disease were studied. Initial examination of IR scans appeared to show a higher level of atrophy than CT scans, but if the scans were windowed to highlight the gray–white matter junction or if SR scans were examined, the comparison with CT was close. The same basic criteria were

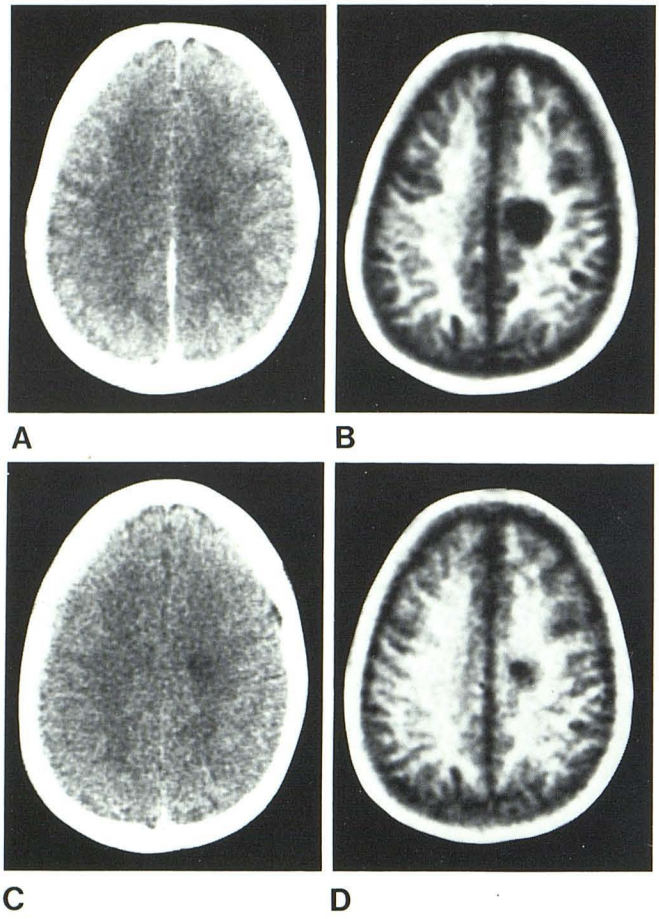

Fig. 22.—Acute multiple sclerosis. **A**, Initial contrast enhanced CT. **B**, $IR_{1400/400}$. Low attenuation area on CT scan (**A**) corresponds in position to lesion seen on NMR scan. (**B**). **C**, Follow-up CT. **D**, $IR_{1400/400}$. Lesion has diminished.

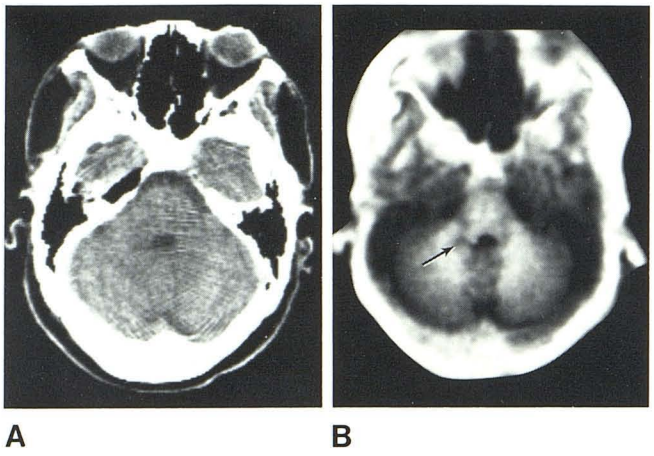

Fig. 23.—Multiple sclerosis: patient with facial myokymia. **A**, CT. **B**, $IR_{1400/400}$. Lesion in pons just lateral to pontomedullary sulcus within lower pontine slice (*arrow*).

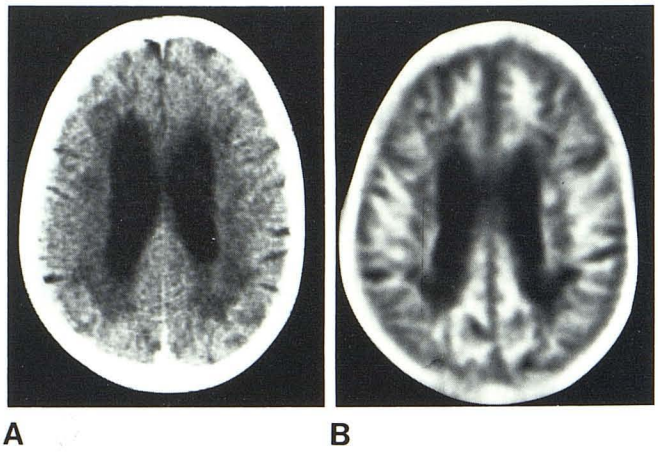

Fig. 24.—Binswanger disease. **A**, CT. **B**, $IR_{1400/400}$. Extensive white matter involvement seen on both scans.

used for both, except that the subarachnoid space generally appeared more extensive on NMR.

In cases of primary cerebral atrophy, Parkinson disease, and Huntington chorea, both gray- and white-matter components appeared to be lost. More selective loss of gray matter was noted in a 54-year-old patient with pre-senile dementia.

In addition to the case of hereditary ataxia, cases of primary cerebellar degeneration of late onset were examined. They showed atrophy of the vermis and the cerebellar hemispheres.

In two cases of motor neurone disease, no abnormality was seen. In a third, with left-sided bulbar signs and lower motor neuron weakness in the left arm, a mild degree of atrophy of this side of the cervical cord was seen. In a fourth patient, a possible enlargement of the basal cisterns around the brainstem was noted.

Other Diseases

There were patients with a variety of other conditions and those in whom a definitive diagnosis was not made. In a patient who had a shunt operation for normal pressure hydrocephalus 4 months earlier, bilateral subdural hygromas were demonstrated (fig. 35). In Paget disease, the soft-tissue component of the disease within the skull was demonstrated (fig. 36).

A 33-year-old patient with a 2 year history of poorly controlled left-sided focal epilepsy showed a mass effect on CT (fig. 37A), but no evidence either with or without contrast enhancement of an underlying space-occupying lesion. $IR_{1400/400}$ and $IR_{1200/200}$ scans (figs. 37B and 37C) demonstrated a lesion in an appropriate position, although it was not biopsied.

A 13-month-old infant with a history of cervical cord damage during breech delivery showed no evidence of a focal abnormality in the brain but very much less cerebral white matter than in adults. A 7-week-old infant with a history of a single fit after delivery showed even less white matter (fig. 38).

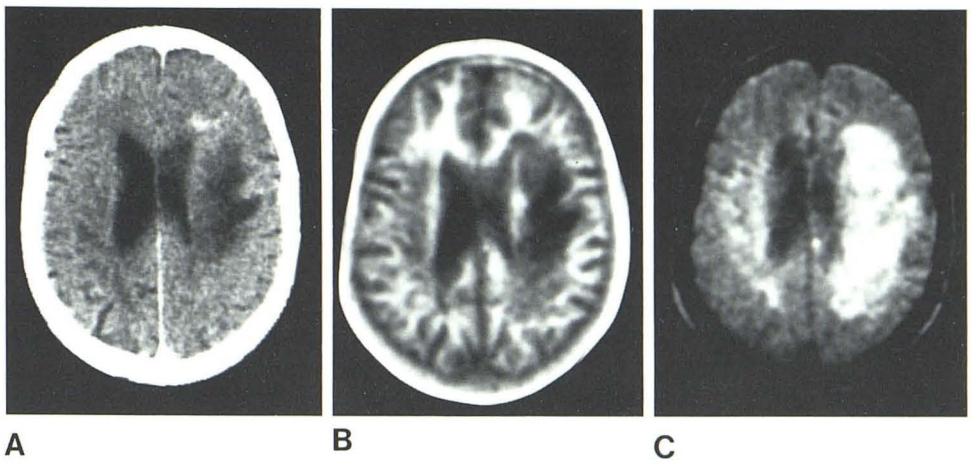

Fig. 25.—Hydrocephalus with periventricular edema. **A**, Contrast-enhanced CT. **B**, $IR_{1400/400}$. **C**, $SE_{1080/40}$. Right hemisphere tumor impinges on right lateral ventricle. Increased T_2 regions seen at margins of both lateral ventricles.

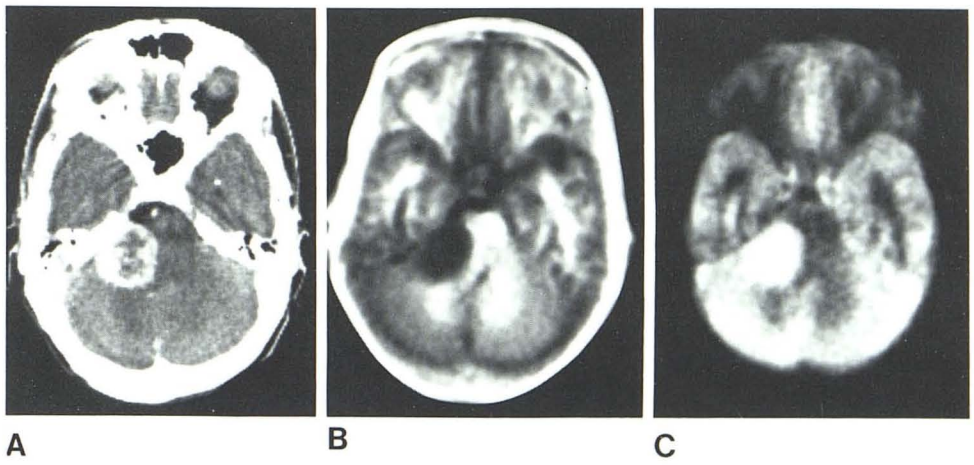

Fig. 26.—Acoustic neuroma. **A**, Contrast-enhanced CT. **B**, $IR_{1400/400}$. **C**, $IR_{1200/200}$. Tumor has long T_1 and appears dark on **B** but light on **C**.

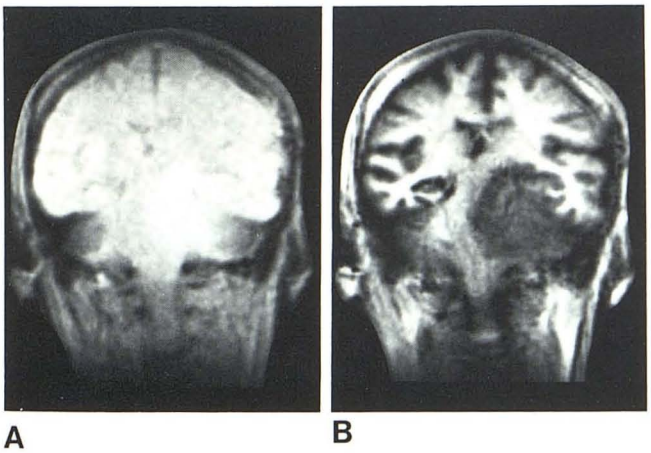

Fig. 27.—Sphenoidal ridge meningioma. **A**, Contrast SR_{1000}. **B**, Contrast $IR_{1400/400}$. Tumor displaces brainstem.

TABLE 5: **Tumors: T_1 Values**

Tumor	No. Cases	T_1 Range (msec)
Meningioma	3	520–600
Acoustic neuroma:		
Noncystic	2	570–700
Cystic	1	1070
Prolactinoma	1	580
Glioma	3	750–1520
Metastasis	7	510–1370

Normal Scans

Normal scans were recorded in cases of suspected multiple sclerosis (three), benign intracranial hypertension (not including SE scans), Behcet disease, Steele-Richardson syndrome, suspected encephalitis, and suspected methotrexate leukonencephalopathy. No abnormality was demonstrated with CT in any of these cases.

Discussion

The sensitivity of NMR imaging to pathologic change in a broad spectrum of neurologic disease is clear. Lesions are demonstrated on IR scans with the background anatomic detail as well as on SE scans where they are highlighted by

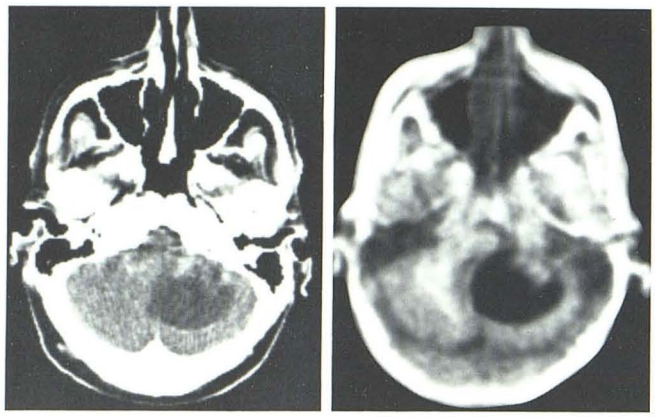

A B

Fig. 28.—Glioma. **A**, CT. **B**, $IR_{1400/400}$. Lighter area within tumor possibly represents hemorrhage. Displacement of brainstem well seen.

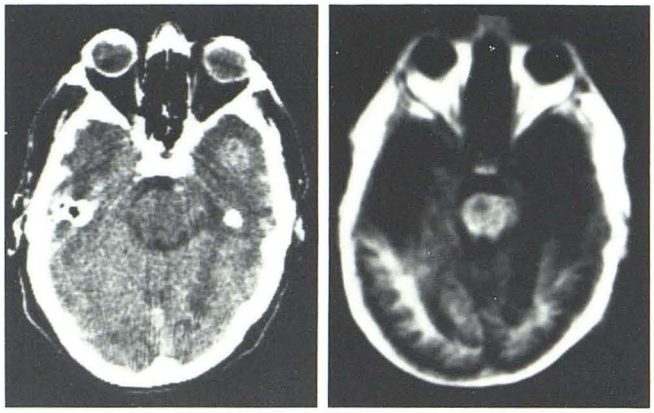

A B

Fig. 31.—Possible brainstem metastasis. **A**, Contrast-enhanced CT. **B**, $IR_{1400/400}$. Long T_1 region within mesencephalon. Metastases and edema in both temporal lobes.

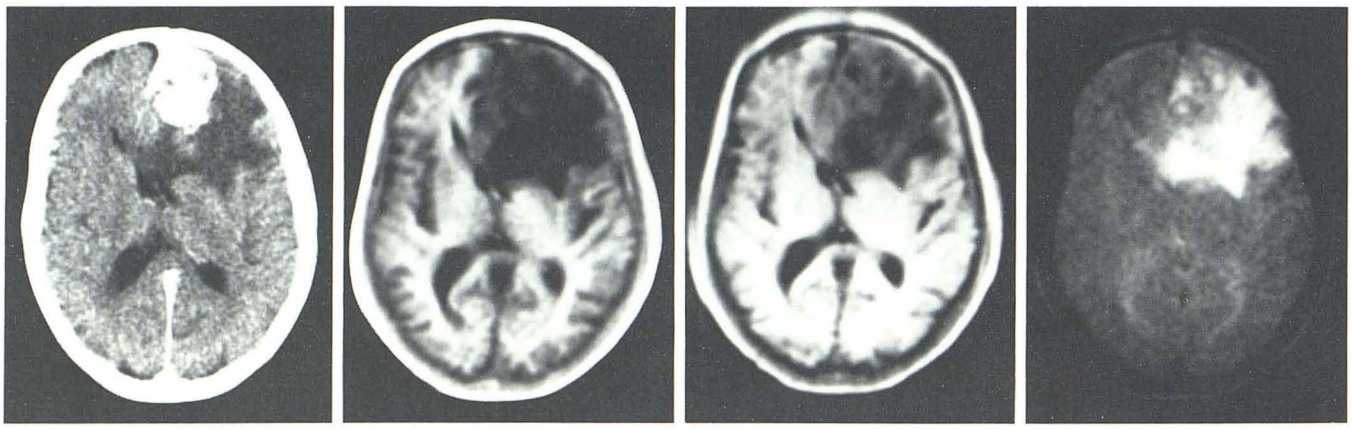

A B C D

Fig. 29.—Metastasis from nasopharyngeal carcinoma. **A**, Contrast-enhanced CT. **B**, $IR_{1400/400}$. **C**, $IR_{2400/800}$. **D**, $SE_{1080/40}$. Margin between tumor and surrounding edema poorly defined in **B**, although it is slightly clearer in **C**. Cerebral edema better defined in **D**.

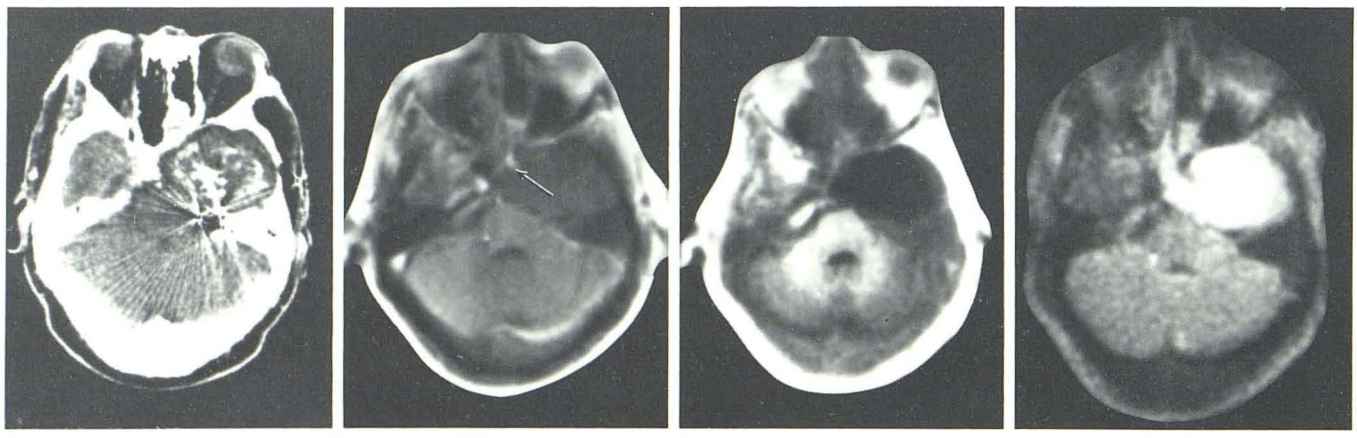

A B C D

Fig. 30.—Epidermoid tumor after incomplete resection. **A**, Contrast enhanced CT. **B**, SR_{300}. **C**, $IR_{1400/400}$. **D**, $SE_{1080/40}$. CT scan (**A**) shows partially calcified tumor together with artifact from metal clip. Displacement of right internal carotid seen in **B** (*arrow*). Tumor defined in **C** and **D**.

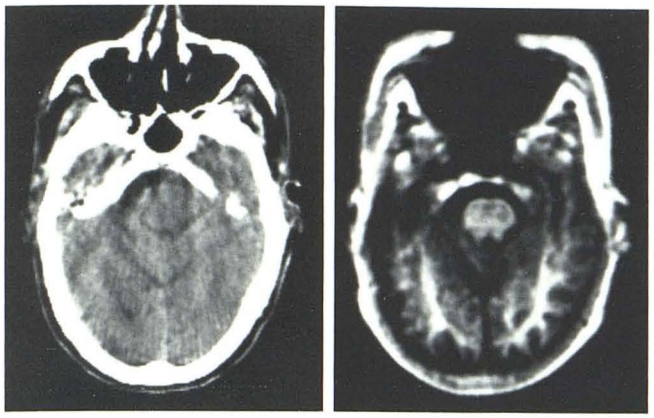

A B

Fig. 32.—Parkinson disease (probably postencephalitic). **A**, CT. **B**, $IR_{1400/400}$. Irregular dark areas within upper mesencephalon.

A B

Fig. 33.—Huntington chorea. **A**, CT. **B**, $IR_{1400/400}$. Heads of caudate nuclei not visible.

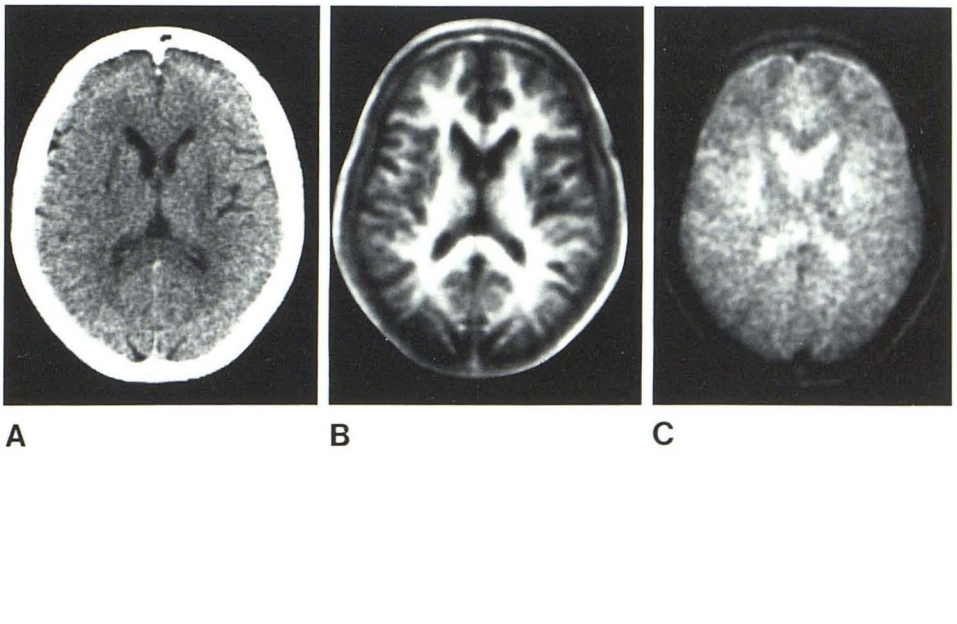

A B C

Fig. 34.—Wilson disease. **A**, CT. **B**, $IR_{1400/400}$. **C**, $SE_{1080/40}$. Long T_1 (**B**) and T_2 (**C**) areas within lenticular nuclei.

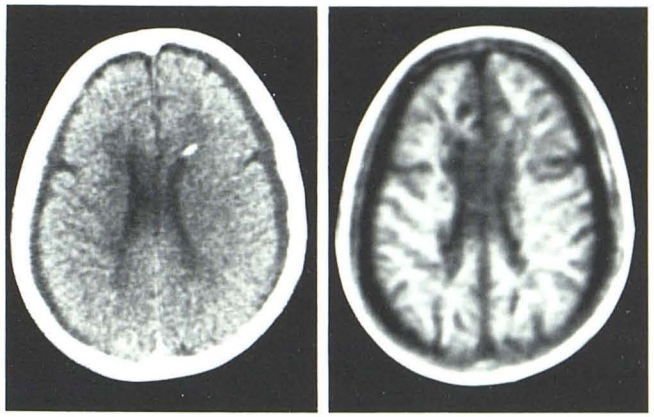

A B

Fig. 35.—Subdural hygroma. **A**, CT. **B**, $IR_{1400/400}$. Low attenuation regions lateral to hemispheres (**A**) corresponding to very long T_1 regions on NMR scan (**B**).

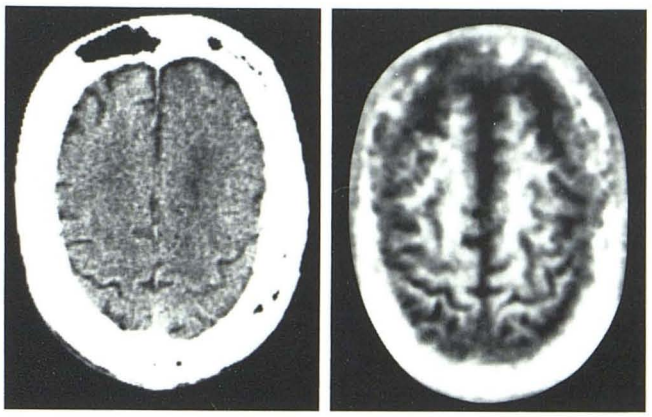

A B

Fig. 36.—Paget disease. **A**, CT. **B**, $IR_{1400/400}$. Enlarged skull vault seen on CT (**A**). Soft-tissue components within this shown on NMR scan (**B**).

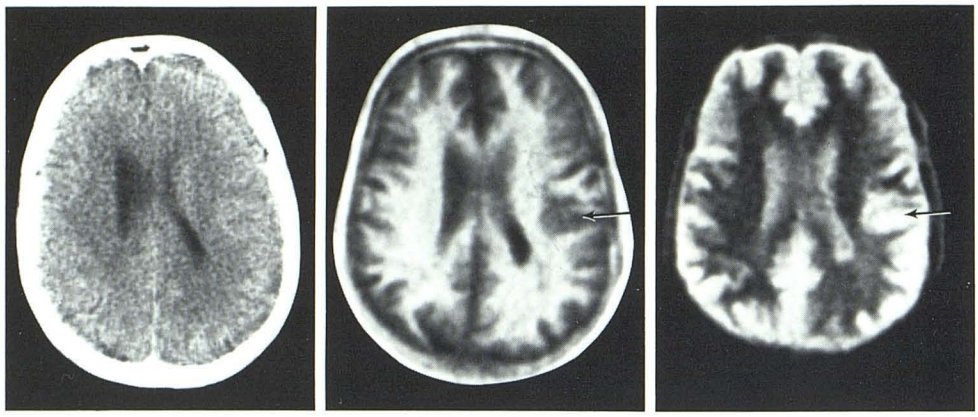

Fig. 37.—Space-occupying lesion. **A**, CT. **B**, $IR_{1400/400}$. **C**, $IR_{1200/200}$. Medial displacement of right lateral margin of lateral ventricle seen on CT scan (**A**). In addition, long T_1 lesion seen on IR scans (*arrows*).

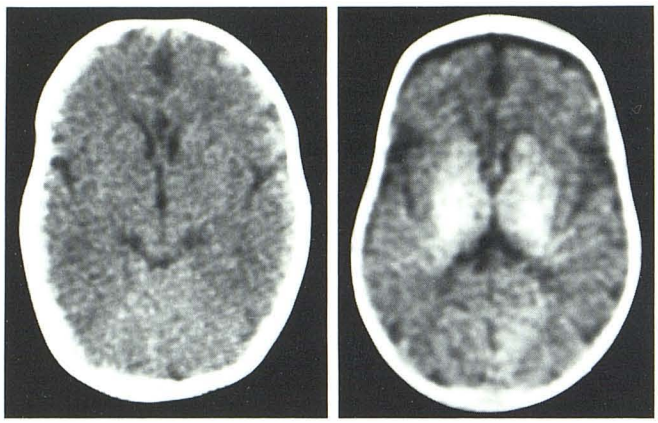

Fig. 38.—CT (**A**) and $IR_{1400/400}$ (**B**) scans in 7-week-old infant. White matter seen only in central regions of brain.

the relatively featureless appearance of the remaining brain. While in some instances NMR duplicates the information from CT, there are also a number of important differences.

Correlation of NMR with CT

In cerebral infarction within the hemispheres, NMR appearances generally paralleled those described for CT [21], except that the loss of gray–white matter contrast could be seen on IR scans without an associated change on the CT scan. While demyelination may occur specifically in Binswanger disease as well as in cerebral anoxia [22] and carbon monoxide poisoning [23] raising the possibility that the loss of gray–white matter contrast may be a result of ischemia or edema in white matter, the basis for this appearance is uncertain at present. Studies of transient ischemic attacks and areas of vasospasm after subarachnoid hemorrhage will be of considerable interest in this context.

The accuracy and time course of CT changes in intracerebral hemorrhage are well established [24]; however, the short T_1 rim and central long T_1 areas seen on IR scans are of interest. It is possible that these latter regions represent central liquefaction. It has been recognized that stages of organization and resolution of intracerebral hemorrhage may simulate normal brain density and thus not be recognised on CT [25], although ring enhancement in intracerebral hemorrhage has been described [26].

Subarachnoid hemorrhage can be seen with CT [27] and may influence the site of angiography [28]. It is possible that IR scans may be useful in detecting hemorrhage in the subarachnoid space adjacent to bone, the basal cisterns, and the posterior fossa where partial-volume effects and artifacts from bone are a problem with CT.

Although subdural hemorrhage is generally well demonstrated with CT, there are particular problems associated with isodense hematomas [29, 30]. It is unlikely that this type of difficulty will be a major problem with NMR. The lateral margin of the hematoma is not obscured by bone artifact, and the medial margin is not likely to be isodense with both white and gray matter unless there is considerable associated cerebral edema. Additional signs of subdural mass effect, including displacement of the gray–white matter interface which may be seen with CT [31], are likely to be much more obvious with IR scans. Internal structure within the hematoma, as seen with intracerebral cases, is likely to add to the visibility of the hematoma. Spin-echo scans offer a further sensitive technique for detecting subdural hemorrhage and any associated edema.

Some problems with CT, such as distinguishing between calcification and acute hemorrhage, both of which may produce high attenuation lesions, may be simply resolved with $IR_{1400/400}$ and SE scans. On these scans, acute hemorrhage appears white due to its short T_1 and long T_2, but calcium appears dark due to its low proton density.

The use of specific sequences to highlight blood flow was of value in arteriovenous malformation and provides a basis for direct flow measurements in these lesions. The venous sinuses are well shown, and occlusion of these should be readily demonstrable with these sequences.

CT has an established role in detecting the early compli-

cations of trauma (including intracranial haematoma), but NMR may be of particular value in showing white-matter shearing injuries and injuries to the brainstem.

NMR may have advantages in detecting lesions in herpes encephalitis, where there may be only a subtle decrease in attenuation with CT and the temporal lobes can be partially obscured by bone artifact.

The lesions of multiple sclerosis are well demonstrated with NMR. Since our earlier report on the use of NMR in multiple sclerosis [13], the improved slice profile has led to an improvement in picture quality with better resolution. Lesions have also been demonstrated with spin-echo sequences, and follow-up has shown a decrease in their size. The patient with facial myokymia (which may be due to multiple sclerosis or pontine tumor [32]) illustrates the use of IR scans for lesion localization. Additional periventricular lesions were seen in this patient, supporting the diagnosis of multiple sclerosis.

Hydrocephalus was equally well seen with NMR and CT, although the fourth ventricle is usually better defined by NMR. The cerebral aqueduct may occasionally be seen. While periventricular edema is particularly well seen with SE scans, sufficient experience has not yet been accumulated to assess how NMR may contribute to the differential diagnosis of the equivalent of periventricular lucency seen with CT.

Although there are some problems in the diagnosis of meningioma with CT, the overall accuracy is high [33, 34]. The tumors in this study were readily identified with both CT and NMR. There was little problem in defining the margin of the tumor from surrounding edema with benign tumors because of their short T_1 and low degree of edema. The high level of accuracy of CT in acoustic neuroma is also well established [35, 36]. In two cases, these tumors were more readily recognized with NMR by displacement of the pons and cerebellum rather than appearances of the tumor itself.

The T_1 values of malignant tumors overlapped those of benign tumors. Here edema was more extensive; with the longer T_1 values, defining the margin of the tumor and surrounding edema was difficult, although mass effects were better demonstrated. The detectability of a tumor depends on its site, and long T_1 lesions are more readily appreciated within the brainstem and deep white matter of the brain than in the gray matter. There is probably a place for a contrast agent to act as a marker of brain-barrier disruption in NMR in a similar way to water-soluble iodinated contrast agents in CT. SE sequences may provide an alternative approach to this problem, since the margin between tumor and surrounding edema was much better defined in the cases studied with the spin-echo sequence.

The capacity of NMR to define the lateral margin of the caudate nucleus allows measurements of the area of the head of this nucleus in order to assess the degree of atrophy in Huntington chorea. This is potentially a more sensitive index of change than the linear measurements previously used in CT [37, 38]. It is also possible that area measurements or T_1 and T_2 values may have some predictive value in family members at risk.

The demonstration of changes in Wilson disease is of interest. Findings have been described with CT [39, 40], but the anatomic relations and definition of the changes are better seen with NMR. This is of interest as a disease of gray matter that is demonstrated with NMR as well as white matter diseases.

While cerebral atrophy is equally well demonstrated with CT and NMR, the absence of artifact in the posterior fossa enables atrophy of the cerebellum to be seen more clearly.

Although both of the infants scanned in this study were potentially abnormal, it is also possible that the lack of white matter was physiologic and that NMR may be a sensitive means of assessing the degree of myelination during the first years of life and thus be of considerable potential value in monitoring cerebral maturation.

TABLE 6: **Basic NMR Signs**

Technique	Signs
Inversion-recovery scans	Focal change in T_1.
	Focal loss of gray–white matter contrast.
	Diffuse or multifocal increase in white matter T_1.
	Diffuse or multifocal increase in gray matter T_1.
	Agenesis atrophy or destruction of gray matter, white matter, or both.
	Mass effects, displacements.
	Hydrocephalus.
Spin-echo scans	Focal increase in T_2.
Saturation-recovery scans	Focal increase in proton density.
	Focal large increase in T_1.
	Flow effects.

TABLE 7: **Focal Change in T_1: Etiology**

Length of T_1	Cause
Short (about white-matter level)	Hemorrhage (acute), blood clot
Long (about gray-matter level or longer)	Infarction, hemorrhage (chronic), arteriovenous malformation, abscess, demyelinating disease, edema, tumor
Very long (about CSF level)	Cyst, subdural hygroma

NMR Signs and Interpretation

NMR signs recognized in this study are summarized in table 6, and a tentative basis for image interpretation is outlined below. With $IR_{1400/400}$ scans, focal lesions were grouped into short T_1 (about that of white matter), long T_1 (about that of gray matter or longer), and very long T_1 (about that of CSF) categories. The associated pathologic changes are shown in table 7. The change in T_1 value in itself was relatively nonspecific, and other factors need to be considered in order to distinguish different types of pathology. With SE scans, focal increases in T_2 are produced by several pathologic processes (table 8). These entities also alter SR scans (table 9).

TABLE 8: **Focal Increase in T_2: Etiology**

Infarction
Hemorrhage
Demyelinating disease
Cerebral edema
Tumor

TABLE 9: **Changes in Saturation-Recovery Scans**

Change	Cause
Increased proton density (relative to brain)	Hemorrhage, acute infarction, edema, tumor
Long or very long T_1	Chronic infarction, tumor, subdural hygroma, cysts

Loss of gray–white matter contrast was seen in cerebral edema, infarction, trauma, and Sturge-Weber disease. Multifocal or diffuse white matter disease was seen in multiple sclerosis and Binswanger disease, and multifocal or diffuse gray matter disease was seen in Huntington chorea and Wilson disease.

Agenesis, atrophy, or destruction was demonstrated in a similar way to CT but, as shown in the two cases of neurosyphylis, this may be relatively selective for white or gray matter.

Mass effects and displacements are also demonstrated in a similar way to CT, but the gray-white margins provide further anatomical landmarks, and the capacity to see the margin of the brainstem and cerebellum in the posterior fossa is also valuable. Sagittal and coronal images can also be used to show displacements.

Hydrocephalus is shown in a similar way to CT, except that periventricular edema may be better demonstrated with SE sequences.

Relative Advantages of NMR

The features of NMR imaging in relation to CT and other techniques require consideration. The high level of gray–white matter contrast is of fundamental importance. Although improvements in CT technology have led to the demonstration of gray- and white-matter differences with third- and fourth-generation CT machines, this is not on the same scale as gray–white matter differences seen with NMR. The level of contrast achieved with NMR equals that of direct visual inspection of the brain and provides a solid basis for localization of lesions as well as assessing mass effects.

The absence of bone artifact allows the margins of the hemispheres to be seen but is of particular value just beneath the calvaria at the base of the brain and in the posterior fossa. Unlike CT, where small proportions of bone within a slice obscure the brain and CSF within the rest of that slice, partial-volume effects from bone are not a major problem with NMR.

The variety of sequences is another advantage of NMR. Although the $IR_{1400/400}$ sequence was used for most purposes, the $IR_{2400/800}$ sequence was useful for lesions with a longer T_1, and the $IR_{1200/200}$ sequence was of value in peripheral lesions and distinguishing regions with a long T_1 from those with a low proton density. SE scans with different values provide a variety of different appearances, and SR images are useful for demonstrating flow effects.

Sagittal and coronal imaging is another valuable feature of NMR. Sagittal images are useful for demonstrating anatomic relations of midline structures, craniovertebral anomalies, and displacements and also display intevertebral disks with a clarity not possible with transverse images.

NMR is sensitive to a wide variety of pathologic change. The increased T_1 found in white matter with demyelination is of importance not just in the demyelinating disease but in the wide variety of other conditions in which demyelination is a feature of the pathologic process. In addition, hemorrhage appears to show specific features, and other pathologic processes, including edema, infection, malignancy, and degenerative change, produce readily discernible changes. Spin-echo sequences appear singularly sensitive to changes in cerebral edema.

The lack of known hazard associated with NMR [41, 42] makes it of particular value in conditions requiring repeated follow-up as well as in pediatric practice.

Disadvantages include the lack of bone detail. It is quite clear that bone changes associated with disease will have to be demonstrated by other techniques, although NMR does offer the possibility of specifically depicting the noncalcified components of bone.

The limited spatial resolution of NMR means that in situations where precise anatomic detail is required, such as small aneurysms, angiography will still be necessary. There are also other areas, such as the pituitary fossa, where the higher resolution of CT gives it an important advantage.

Contrast-enhanced CT is of value in demonstrating areas where there is breakdown of the blood-brain barrier which can be depicted using iodinated contrast agents. Preliminary work has shown that paramagnetic agents, such as molecular oxygen, ferric chloride, and manganese, can be used to enhance spin-lattice relaxation. Such inquiries suggest an optimistic future for the development of contrast agents for NMR.

The basic cost of an NMR unit is likely to be high and to parallel that of CT units. At present, NMR scanning is slow, with a typical scan time of 4.2 min per slice. Multiple-slice options enabling several slices to be obtained simultaneously are now being developed.

Much more work remains to be done in order to assess the role of NMR in neurologic practice, and there is not a single disease grouping included in this series that would not benefit from further study. Opportunities for further investigation have been suggested above, but there are a number of other extensions of this work that might prove just as rewarding.

The capacity to demonstrate myelin formation in the developing infant and the lack of known hazards suggest the technique may be useful in evaluating brain maturation in children, although a cautious attitude is probably justified

concerning the possibility of long-term hazards. NMR of the leukodystrophies and other conditions in which low CT attenuation lesions occur in childhood is also likely to be rewarding. The sensitivity of spin-echo scans to changes in edema may also be of value in the assessment of anoxic-ischemic brain damage in which the limitations of CT are well known [43, 44].

Measurements of T_1 and T_2 may be of value in tissue characterization and in following the evolution of disease and response to therapy.

In addition to multiple sclerosis, a variety of other demyelinating diseases in which abnormalities have been demonstrated with CT, such as methotrexate encephalopathy, myelinolysis, progressive multifocal leukoencephalopathy, and anoxic damage, should be well demonstrated with IR scans.

There is also a variety of other conditions (such as the encephalitides) in which CT may show only minor or subtle abnormalities in which NMR should be of greater value.

CT has undoubtedly provided a major stimulus for the development of NMR. Direct comparison with established CT appearances on a slice-by-slice basis has also permitted a rapid appreciation of the NMR features of a wide range of diseases. However, detailed evaluation of CT and NMR results, on a disease-by-disease basis and over an extended period, will be necessary to identify the optimum application of each. In a wider context, the recent introduction of CT as variously perceived by commercial interests, regulatory agencies, insurers, patients, clinicians, and radiologists is likely to have a major influence on the development of NMR.

ACKNOWLEDGMENTS

We thank the Department of Health and Social Security, and in particular Gordon Higson and John Williams for their continued support and encouragement. We also thank our clinical colleagues for their help in referring cases to us.

REFERENCES

1. Damadian R. Tumor detection by nuclear magnetic resonance. *Science* **1971**;171:1151–1153
2. Lauterbur PC. Image formation by induced local interactions: examples employing nuclear magnetic resonance. *Nature* **1973**;242:190–191
3. Mallard J. The noes have it! Do they? *Br J Radiol* **1981**; 54:831–849
4. Andrew ER. NMR imageing of intact biological systems. *Philos Trans R Soc Lond [Biol]* **1980**;289:471–481
5. Hounsfield GN. Computed medical imaging. *J Comput Assist Tomogr* **1980**;4:665–674
6. Holland GN, Moore WS, Hawkes RC. Nuclear magnetic resonance tomography of the brain. *J Comput Assist Tomogr* **1980**;4:1–3
7. Moore WS, Holland GN, Kreel L. The NMR CAT scanner—a new look at the brain. *CT* **1980**;4:1–7
8. Moore WS, Holland GN. Nuclear magnetic resonance imaging. *Br Med Bull* **1980**;36:297–299
9. Holland GN, Hawkes RC, Moore WS. Nuclear magnetic resonance (NMR) tomography of the brain: coronal and sagittal sections. *J Comput Assist Tomogr* **1980**;4:429–433
10. Hawkes RC, Holland GN, Moore WS, Worthington BS. Nuclear magnetic resonance (NMR) tomography of the brain: a preliminary clinical assessment with demonstration of pathology. *J Comput Assist Tomogr* **1980**;4:577–586
11. Edelstein WA, Hutchison JMS, Smith FW, Mallard J, Johnson G, Redpath TW. Human whole body NMR tomographic imaging: normal sections. *Br J Radiol* **1981**;54:149–151
12. Besson JAO, Glen AIM, Foreman EI, et al. Nuclear magnetic resonance observations in alcoholic cerebral disorder and the role of vasopressin. *Lancet* **1981**;2:923–934
13. Young IR, Hall AS, Pallis CA, Legg NJ, Bydder GM, Steiner RE. Nuclear magnetic resonance imaging of the brain in multiple sclerosis. *Lancet* **1981**;2:1063–1066
14. Doyle FH, Gore JC, Pennock JM, et al. Imaging of the brain by nuclear magnetic resonance. *Lancet* **1981**;2:53–57
15. Young IR, Burl M, Clarke GJ, et al. Magnetic resonance properties of hydrogen: imaging the posterior fossa. *AJR* **1981**;137:895–901, *AJNR* **1981**;2:487–493
16. National Radiological Protection Board. *Exposure to nuclear magnetic resonance clinical imaging.* **1980**. (Available from the Secretary, NRPB, Harwell, Oxon OX11 ORQ, UK)
17. Doyle FH, Pennock JM, Banks LM, et al. Nuclear magnetic resonance (NMR) imaging of the liver. *AJR* **1982**;138:193–200
18. Young IR, Bailes DR, Collins AG, Gilderdale DJ. Image options in NMR. In: Witcofski RL, Karstaedt N, Partain CL, eds. *NMR imaging.* Winston-Salem: Bowman Gray School of Medicine, **1982**:93–100
19. Le May M, Kido DK. Asymmetries of the cerebral hemispheres on computed tomograms. *J Comput Assist Tomogr* **1978**; 2:471–476
20. Steele JR, Hoffman JC. Brainstem evaluation with CT cisternography. *AJR* **1981**;136:287–292
21. Davis KR, Taveras JM, New PFJ, Schnur JA, Roberson GH. Cerebral infarction diagnosis by computerised tomography. *AJR* **1975**;124:643–660
22. Yagnik P, Gonzalez C. White matter involvement in anoxic encephalopathy in adults. *J Comput Assist Tomogr* **1980**; 4:788–790
23. Kim KS, Weinberg PE, Suh JH, Sam UH. Acute carbon monoxide poisoning: Computed tomography of the brain. *AJNR* **1980**;1:399–402
24. Dolinskas CA, Bilaniuk LT, Zimmerman RA, Kuhl DE. Computed tomography of intracerebral haematomas. I. Transmission CT observations on hematoma resolution. *AJR* **1977**; 129:681–688
25. Messina AV, Chernik NL. Computed tomography: the "resolving" intracerebral haemorrhage. *Radiology* **1975**; 118:609–613
26. Zimmerman RD, Leeds NE, Naidich TP. Ring blush associated with intracerebral hematoma. *Radiology* **1977**;122:707–711
27. Sim ST, Sage DJ. Detection of subarachnoid blood clot and other thin flat structures by computed tomography. *Radiology* **1977**;123:79–84
28. Kendall BE, Lee BCP, Claveria E. Computerized tomography and angiography in subarachnoid haemorrhage. *Br J Radiol* **1976**;49:483–501
29. Amendola A, Ostrum BJ. Diagnosis of isodense subdural hematomas by computed tomography. *AJR* **1977**;129:693–697
30. Moller A, Ericson K. Computed tomography of isoattenuating subdural hematomas. *Radiology* **1979**;130:149–152
31. Barmeir E, Dubowitz B. Grey-white matter interface (G-WMI) displacement. A new sign in the computed tomographic diagnosis of subtle subdural haematomas. *Clin Radiol* **1981**;32:393–396
32. Mathews WB. Facial myokymia. *J Neurol Neurosurg Psychiatry*

1966;29:35–39
33. New PFJ, Aronow S, Hesselink JR. National Cancer Institute Study: Evaluation of computed tomography in the diagnosis of intracranial neoplasms. IV. Meningiomas. *Radiology* **1980**; 136:665–675
34. Pullicino P, Kendall BE, Jakubowski J. Difficulties in diagnosis of intracranial meningiomas by computed tomography. *J Neurol Neurosurg Psychiatry* **1980**;43:1022–1029
35. Robbins B, Marshall WH. Computed tomography of acoustic neurinoma. *Radiology* **1978**;128:367–370
36. Thomson JLG. Computerised axial tomography in posterior fossa lesions. *Clin Radiol* **1978**;29:233–250
37. Neophytides AN, Di Chiro G, Barron SA, Chase TN. Computed axial tomography in Huntington's disease and persons at risk for Huntington's disease. *Adv Neurol* **1979**;23:185–191
38. Terrence CF, Delaney JF, Alberts MC. Computed tomography for Huntington's disease. *Neuroradiology* **1977**;13:173–175
39. Hank SI, Post MJD. Computed tomography in Wilson's disease. *Neurology* **1981**;31:107–110
40. Kendall BE, Pollock SE, Bass NM, Valentine AR. Wilson's disease. Clinical correlation with cranial computed tomography. *Neuroradiology* **1982**;22:1–5
41. Budinger TF. Nuclear magnetic resonance (NMR) in vivo studies. Known thresholds for health effects. *J Comput Assist Tomogr* **1981**;5:800–811
42. Saunders RD. The biological hazards of NMR. In: Witcofski RL, Karstaedt N, Partain CL, eds. *NMR imaging*. Winston-Salem: Bowman Gray School of Medicine, **1982**:65–71
43. Flodmark O, Becker LE, Harwood-Nash DC, Fitzhardinge PM, Fitz CR, Chuang SH. Correlation between computed tomography and autopsy in premature and full-term neonates that have suffered perinatal asphyxia. *Radiology* **1980**;137:93–103
44. Flodmark O, Fitz DR, Harwood-Nash DC. CT diagnosis and short-term prognosis of intracranial haemorrhage and hypoxic/ischemic brain damage in neonates. *J Comput Assist Tomogr* **1980**;4:775–778